Astronomy & Astrophysics

21 cm observation of large-scale structures at *z* ∼ 1

Instrument sensitivity and foreground subtraction

R. Ansari[1,2], J. E. Campagne[2], P. Colom[3], J. M. Le Goff[4], C. Magneville[4],
J. M. Martin[5], M. Moniez[2], J. Rich[4], and C. Yèche[4]

[1] Université Paris-Sud, LAL, UMR 8607, CNRS/IN2P3, 91405 Orsay, France
   e-mail: ansari@lal.in2p3.fr
[2] CNRS/IN2P3, Laboratoire de l'Accélérateur Linéaire (LAL), BP 34, 91898 Orsay Cedex, France
[3] LESIA, UMR 8109, Observatoire de Paris, 5 place Jules Janssen, 92195 Meudon Cedex, France
[4] CEA, DSM/IRFU, Centre d'Études de Saclay, 91191 Gif-sur-Yvette, France
[5] GEPI, UMR 8111, Observatoire de Paris, 61 Ave. de l'Observatoire, 75014 Paris, France

ABSTRACT

Context. Large-scale structures (LSS) in the universe can be traced using the neutral atomic hydrogen H_I through its 21 cm emission. Such a 3D matter distribution map can be used to test the cosmological model and to constrain the dark energy properties or its equation of state. A novel approach, called intensity mapping, can be used to map the H_I distribution, using radio interferometers with a large instantaneous field of view and waveband.

Aims. We study the sensitivity of different radio interferometer configurations, or multi-beam instruments for observing LSS and baryon acoustic oscillations (BAO) in 21 cm, and we discuss the problem of foreground removal.

Methods. For each configuration, we determined instrument response by computing the (u, v) or Fourier angular frequency plane coverage using visibilities. The (u, v) plane response determines the noise power spectrum, hence the instrument sensitivity for LSS $P(k)$ measurement. We also describe a simple foreground subtraction method of separating LSS 21 cm signal from the foreground due to the galactic synchrotron and radio source emission.

Results. We have computed the noise power spectrum for different instrument configurations, as well as the extracted LSS power spectrum, after separating the 21 cm-LSS signal from the foregrounds. We have also obtained the uncertainties on the dark energy parameters for an optimized 21 cm BAO survey.

Conclusions. We show that a radio instrument with few hundred simultaneous beams and a collecting area of ∼10 000 m² will be able to detect BAO signal at redshift *z* ∼ 1 and will be competitive with optical surveys.

Key words. large-scale structure of Universe – dark energy – instrumentation: interferometers – radio lines: galaxies – radio continuum: general

1. Introduction

The study of the statistical properties of large-scale structures (LSS) in the Universe and of their evolution with redshift is one of the major tools in observational cosmology. These structures are usually mapped through optical observation of galaxies that are used as tracers of the underlying matter distribution. An alternative and elegant approach for mapping the matter distribution, which uses neutral atomic hydrogen (H_I) as a tracer with intensity mapping, has been proposed in recent years (Peterson et al. 2006; Chang et al. 2008). Mapping the matter distribution using H_I 21 cm emission as a tracer has been extensively discussed in the literature (Furlanetto et al. 2006; Tegmark & Zaldarriaga 2009) and is being used in projects such as LOFAR (Rottering et al. 2006) or MWA (Bowman et al. 2007) to observe reionization at redshifts *z* ∼ 10.

Evidence of the acceleration in the expansion of the universe has accumulated over the past twelve years, thanks to the observation of distant supernovae and cosmic microwave background (CMB) anisotropies and to detailed analysis of the LSS. A cosmological constant (Λ) or new cosmological energy density called *dark energy* has been advocated as the origin of this acceleration. Dark energy is considered as one of the most

intriguing puzzles in physics and cosmology. Several cosmological probes can be used to constrain the properties of this new cosmic fluid, more precisely its equation of state: the Hubble diagram, or the luminosity distance as a function of redshift of supernovae as standard candles, galaxy clusters, weak shear observations, and baryon acoustic oscillations (BAO).

BAO are features imprinted in the distribution of galaxies, due to the frozen sound waves that were present in the photon-baryon plasma prior to recombination at *z* ∼ 1100. This scale can be considered as a standard ruler with a comoving length of ∼150 Mpc, and these features have been first observed in the CMB anisotropies and are usually referred to as *acoustic peaks* (Mauskopf et al. 2000; Larson et al. 2011). The BAO modulation has been subsequently observed in the distribution of galaxies at low redshift (*z* < 1) in the galaxy-galaxy correlation function by the SDSS (Eisenstein et al. 2005; Percival et al. 2007; Percival et al. 2010), 2dGFRS (Cole et al. 2005), as well as WiggleZ (Blake et al. 2011) optical galaxy surveys.

Ongoing surveys, such as BOSS (Eisenstein et al. 2011) or future surveys, such as LSST (Abell et al. 2009), plan to measure the BAO scale precisely in the redshift range $0 \lesssim z \lesssim 3$, using either optical observation of galaxies or 3D mapping

of Lyman α absorption lines toward distant quasars (McDonald et al. 2006; McDonald & Eisenstein 2007). Radio observation of the 21 cm emission of neutral hydrogen is a very promising technique for mapping matter distribution up to redshift $z \sim 3$, and it complements optical surveys, especially in the optical redshift desert range $1 \lesssim z \lesssim 2$, and possibly up to the reionization redshift (Wyithe et al. 2008).

In Sect. 2, we discuss the intensity mapping and its potential for measuring the H_I mass-distribution power spectrum. The method used in this paper to characterize a radio instrument response and sensitivity for $P_{H_I}(k)$ is presented in Sect. 3. We also show the results for the 3D noise power spectrum for several instrument configurations. The contribution of foreground emissions due to both the galactic synchrotron and radio sources is described in Sect. 4, as is a simple component separation method. The performance of this method using two different sky models is also presented in Sect. 4. The constraints that can be obtained on the dark energy parameters and DETF figure of merit for typical 21 cm intensity mapping survey are discussed in Sect. 5.

2. Intensity mapping and H$_I$ power spectrum

2.1. 21 cm intensity mapping

Most of the cosmological information in the LSS is located on large scales ($\gtrsim 1$ deg), while the interpretation on the smallest scales might suffer from the uncertainties on the nonlinear clustering effects. The BAO features in particular are at the degree angular scale on the sky and thus can be resolved easily with a rather modest size radio instrument (diameter $D \lesssim 100$ m). The specific BAO clustering scale (k_{BAO}) can be measured both in the transverse plane (angular correlation function, $k_{BAO}^{\perp}$) or along the longitudinal (line of sight or redshift $k_{BAO}^{\parallel}$) direction. A direct measurement of the Hubble parameter $H(z)$ can be obtained by comparing the longitudinal and transverse BAO scales. A reasonably good redshift resolution $\delta z \lesssim 0.01$ is needed to resolve longitudinal BAO clustering, which is a challenge for photometric optical surveys.

To obtain a measurement of the LSS power spectrum with small enough statistical uncertainties (sample or cosmic variance), a large volume of the universe should be observed, typically a few Gpc^3. Moreover, stringent constraint on DE parameters can only be obtained when comparing the distance or Hubble parameter measurements with DE models as a function of redshift, which requires a significant survey depth $\Delta z \gtrsim 1$. Radio instruments intended for BAO surveys must thus have large instantaneous field of view (FOV $\gtrsim 10$ deg^2) and large bandwidth ($\Delta \nu \gtrsim 100$ MHz) to explore large redshift domains.

Although the application of 21 cm radio survey to cosmology, in particular LSS mapping, has been discussed in length in the framework of large future instruments, such as the SKA (e.g. Carilli et al. 2004; Abdalla & Rawlings 2005), the method envisaged has mostly been through the detection of galaxies as H$_I$ compact sources. However, extremely large radio telescopes are required to detected H$_I$ sources at cosmological distances. The sensitivity (or detection threshold) limit S_{lim} for the total power from the two polarizations of a radio instrument characterized by an effective collecting area A, and system temperature T_{sys} can be written as

$$S_{lim} = \frac{\sqrt{2}\, k_B\, T_{sys}}{A\, \sqrt{t_{int} \delta \nu}} \tag{1}$$

where t_{int} is the total integration time and $\delta \nu$ the detection frequency band. In Table 1 (left) we computed the sensitivity for six different sets of instrument effective area and system temperature, with a total integration time of 86 400 s (1 day) over a frequency band of 1 MHz. The width of this frequency band is well adapted to detecting an H$_I$ source with an intrinsic velocity dispersion of a few 100 km s^{-1}. These detection limits should be compared with the expected 21 cm brightness S_{21} of compact sources, which can be computed using the expression below (e.g. Binney & Merrifield 1998):

$$S_{21} \simeq 0.021\,\mu\text{Jy}\,\frac{M_{H_I}}{M_\odot} \times \left(\frac{1\,\text{Mpc}}{d_L(z)}\right)^2 \times \frac{200\,\text{km s}^{-1}}{\sigma_v}(1+z) \tag{2}$$

where M_{H_I} is the neutral hydrogen mass, $d_L(z)$ the luminosity distance, and σ_v the source velocity dispersion. The 1 MHz bandwidth mentioned above is only used for computing the galaxy detection thresholds and does not determine the total bandwidth or frequency resolution of an intensity mapping survey.

In Table 1 (right), we show the 21 cm brightness for compact objects with a total H$_I$ mass of $10^{10}\,M_\odot$ and an intrinsic velocity dispersion of 200 km s^{-1}. The luminosity distance was computed for the standard WMAP ΛCDM universe (Komatsu et al. 2011). From 10^9 to $10^{10}\,M_\odot$ of neutral gas mass is typical of large galaxies (Lah et al. 2009). It is clear that detecting H$_I$ sources at cosmological distances would require collecting area in the range of 10^6 m^2.

Intensity mapping has been suggested as an alternative and economic method of mapping the 3D distribution of neutral hydrogen by (Chang et al. 2008; Ansari et al. 2008; Seo et al. 2010). There have also been attempts to detect the 21 cm LSS signal at GBT (Chang et al. 2010) and at GMRT (Ghosh et al. 2011). In this approach, a sky brightness map with angular resolution $\sim 10-30$ arcmin is created for a wide range of frequencies. Each 3D pixel (2 angles Θ, frequency ν, or wavelength λ) would correspond to a cell with a volume of $\sim 10^3$ Mpc^3, containing ten to a hundred galaxies and a total H$_I$ mass $\sim 10^{12}\,M_\odot$. If we neglect local velocities relative to the Hubble flow, the observed frequency ν would be translated into the emission redshift z through the well known relation

$$z(\nu) = \frac{\nu_{21} - \nu}{\nu}; \ \nu(z) = \frac{\nu_{21}}{(1+z)} \text{ with } \nu_{21} = 1420.4\,\text{MHz} \tag{3}$$

$$z(\lambda) = \frac{\lambda - \lambda_{21}}{\lambda_{21}}; \ \lambda(z) = \lambda_{21} \times (1+z) \text{ with } \lambda_{21} = 0.211\,\text{m.} \tag{4}$$

The large-scale distribution of the neutral hydrogen, down to an angular scale of ~ 10 arcmin can then be observed without detecting individual compact H$_I$ sources, using the set of sky-brightness maps as a function of frequency (3D-brightness map) $B_{21}(\Theta, \lambda)$. The sky brightness B_{21} (radiation power/unit solid angle/unit surface/unit frequency) can be converted to brightness temperature using the Rayleigh-Jeans approximation of black body radiation law:

$$B(T, \lambda) = \frac{2k_B T}{\lambda^2}.$$

2.2. H$_I$ power spectrum and BAO

In the absence of any foreground or background radiation and assuming a high spin temperature, $k_B T_{spin} \gg h\nu_{21}$, the brightness temperature for a given direction and wavelength $T_{21}(\Theta, \lambda)$

Table 1. 21 cm source brightness and detection limits.

$A(m^2)$	$T_{sys}(K)$	$S_{lim}\,\mu Jy$	z	d_L(Mpc)	$S_{21}(\mu Jy)$
5000	50	66	0.25	1235	175
5000	25	33	0.50	2800	40
100 000	50	3.3	1.0	6600	9.6
100 000	25	1.66	1.5	10 980	3.5
500 000	50	0.66	2.0	15 710	2.5
500 000	25	0.33	2.5	20 690	1.7

Notes. *Left panel*: sensitivity or source detection limit for 1-day integration time (86 400 s) and 1-MHz frequency band. *Right panel*: 21 cm brightness for sources containing $10^{10}\,M_\odot$ of H$_I$ at different redshifts.

would be proportional to the local H$_I$ number density $n_{HI}(\Theta, z)$ through the relation (Field 1959; Zaldarriaga et al. 2004):

$$T_{21}(\Theta, \lambda(z)) = \frac{3}{32\pi} \frac{h}{k_B} A_{21} \lambda_{21}^2 \times \frac{c}{H(z)} (1+z)^2 \times n_{HI}(\Theta, z) \quad (5)$$

where $A_{21} = 2.85 \times 10^{-15}$ s^{-1} (Lang 1999) is the spontaneous 21 cm emission coefficient, h the Planck constant, c the speed of light, k_B the Boltzmann constant, and $H(z)$ the Hubble parameter at the emission redshift. For a ΛCDM universe and neglecting radiation energy density, the Hubble parameter can be expressed as

$$H(z) \simeq h_{100} \left[\Omega_m(1+z)^3 + \Omega_\Lambda \right]^{\frac{1}{2}} \times 100 \text{ km s}^{-1} \text{ Mpc}^{-1}. \quad (6)$$

After introducing the H$_I$ mass fraction relative to the total baryon mass f_{H_I}, the neutral hydrogen number density and the corresponding 21 cm emission temperature can be written as a function of H$_I$ relative density fluctuations:

$$n_{HI}(\Theta, z(\lambda)) = f_{H_I}(z) \times \Omega_B \frac{\rho_{crit}}{m_H} \times \left(\frac{\delta\rho_{H_I}}{\bar{\rho}_{H_I}}(\Theta, z) + 1 \right) \quad (7)$$

$$T_{21}(\Theta, \lambda(z)) = \bar{T}_{21}(z) \times \left(\frac{\delta\rho_{H_I}}{\bar{\rho}_{H_I}}(\Theta, z) + 1 \right) \quad (8)$$

where Ω_B and ρ_{crit} are the present-day mean baryon cosmological and critical densities, respectively, m_H the hydrogen atom mass, and $\frac{\delta\rho_{H_I}}{\bar{\rho}_{H_I}}$ the H$_I$ density fluctuations.

The present-day neutral hydrogen fraction $f_{H_I}(0)$ present in local galaxies has been measured to be ~1% of the baryon density (Zwaan et al. 2005)

$$\Omega_{H_I} \simeq 3.5 \times 10^{-4} \sim 0.008 \times \Omega_B.$$

The neutral hydrogen fraction is expected to increase with redshift, as gas is used in star formation during galaxy formation and evolution. Study of Lyman-α absorption indicates a factor 3 increase in the neutral hydrogen fraction at $z = 1.5$ in the intergalactic medium (Wolf et al. 2005), compared to its current value $f_{H_I}(z = 1.5) \sim 0.025$. The 21 cm brightness temperature and the corresponding power spectrum can be written as (Madau et al. 1997; Zaldarriaga et al. 2004; Barkana & Loeb 2007)

$$P_{T_{21}}(k) = \left(\bar{T}_{21}(z) \right)^2 P(k) \quad (9)$$

$$\bar{T}_{21}(z) \simeq 0.084 \text{ mK} \frac{(1+z)^2 h_{100}}{\sqrt{\Omega_m(1+z)^3 + \Omega_\Lambda}} \frac{\Omega_B}{0.044} \frac{f_{H_I}(z)}{0.01}. \quad (10)$$

Table 2 shows the mean 21 cm brightness temperature for the standard ΛCDM cosmology and either a constant H$_I$ mass fraction $f_{H_I} = 0.01$, or linearly increasing $f_{H_I} \simeq 0.008 \times (1+z)$.

Table 2. 21 cm brightness temperature (mK) at different redshifts.

z	0.25	0.5	1.	1.5	2.	2.5	3.
$\bar{T}_{21}{}^a$	0.085	0.107	0.145	0.174	0.195	0.216	0.234
$\bar{T}_{21}{}^b$	0.085	0.128	0.232	0.348	0.468	0.605	0.749

Notes. Mean 21 cm brightness temperature in mK for the standard ΛCDM cosmology as a function of redshift. [a] Constant H$_I$ mass fraction $f_{H_I}(z) = 0.01$. [b] Linearly increasing mass fraction $f_{H_I}(z) = 0.008(1+z)$.
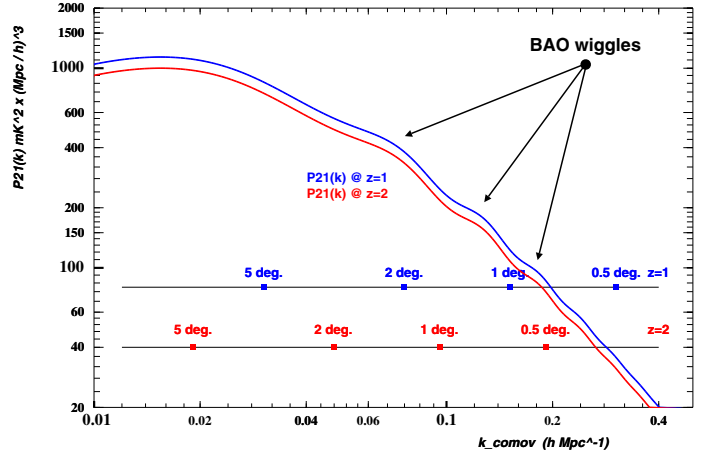

Fig. 1. H$_I$ 21 cm emission power spectrum at redshifts $z = 1$ (blue) and $z = 2$ (red), with neutral gas fraction $f_{H_I} = 2\%$.

Figure 1 shows the 21 cm emission power spectrum at several redshifts, with a constant neutral fraction at 2% ($f_{H_I} = 0.02$). The matter power spectrum has been computed using the Eisenstein & Hu (1998) parametrization. The correspondence with the angular scales is also shown for the standard WMAP ΛCDM cosmology, according to the relation

$$\theta_k = \frac{2\pi}{k\, d_A(z)\,(1+z)}, \quad k = \frac{2\pi}{\theta_k\, d_A(z)\,(1+z)}, \quad (11)$$

where k is the comoving wave vector and $d_A(z)$ is the angular diameter distance. The matter power spectrum $P(k)$ has been measured using galaxy surveys, for example by SDSS and 2dF at low redshift $z \lesssim 0.3$ (Cole et al. 2005; Tegmark et al. 2004). The 21 cm brightness power spectra $P_{T_{21}}(k)$ shown here are comparable to the power spectrum measured from the galaxy surveys, once the mean 21 cm temperature conversion factor $(\bar{T}_{21}(z))^2$, redshift evolution, and different bias factors have been accounted for.

3. Interferometric observations and *P(k)* measurement sensitivity

3.1. Instrument response

We briefly introduce here the principles of interferometric observations and the definition of quantities useful for our calculations. The interested reader may refer to Thompson et al. (2001) for a detailed and complete presentation of observation methods and signal processing in radio astronomy. In astronomy we are usually interested in measuring the sky emission intensity, $I(\Theta, \lambda)$ in a given wave band, as a function of the sky direction. In radio astronomy and interferometry in particular, receivers are sensitive to the sky emission complex amplitudes. However, for

most sources, the phases vary randomly with a spatial correlation length significantly smaller than the instrument resolution,

$$I(\Theta, \lambda) = |A(\Theta, \lambda)|^2, \ I \in \mathbb{R}, A \in \mathbb{C} \tag{12}$$

$$\langle A(\Theta, \lambda)A^*(\Theta', \lambda)\rangle_{\text{time}} = 0 \ \text{ for } \Theta \neq \Theta'. \tag{13}$$

A single receiver can be characterized by its angular complex amplitude response $B(\Theta, \nu)$ and its position $\boldsymbol{r}$ in a reference frame. The waveform complex amplitude s measured by the receiver, for each frequency can be written as a function of the electromagnetic wave vector $\boldsymbol{k}_{\text{EM}}(\Theta, \lambda)$:

$$s(\lambda) = \iint \mathrm{d}\Theta \ A(\Theta, \lambda)B(\Theta, \lambda)\mathrm{e}^{\mathrm{i}(\boldsymbol{k}_{\text{EM}}.\boldsymbol{r})}. \tag{14}$$

We set the electromagnetic (EM) phase origin at the center of the coordinate frame, and the EM wave vector is related to the wavelength λ through the usual equation $|\boldsymbol{k}_{\text{EM}}| = 2\pi/\lambda$. The receiver beam or antenna lobe $L(\Theta, \lambda)$ corresponds to the receiver intensity response:

$$L(\Theta, \lambda) = B(\Theta, \lambda) \, B^*(\Theta, \lambda). \tag{15}$$

The visibility signal of two receivers corresponds to the time-averaged correlation between signals from two receivers. If we assume a sky signal with random uncorrelated phase, the visibility $\mathcal{V}_{12}$ signal from two identical receivers, located at the positions $\boldsymbol{r_1}$ and $\boldsymbol{r_2}$, can simply be written as a function of their position difference $\Delta \boldsymbol{r} = \boldsymbol{r_1} - \boldsymbol{r_2}$

$$\mathcal{V}_{12}(\lambda) = \langle s_1(\lambda)s_2(\lambda)^*\rangle = \iint \mathrm{d}\Theta \ I(\Theta, \lambda)L(\Theta, \lambda)\mathrm{e}^{\mathrm{i}(\boldsymbol{k}_{\text{EM}}.\Delta \boldsymbol{r})}. \tag{16}$$

This expression can be simplified if we consider receivers with a narrow FOV ($L(\Theta, \lambda) \simeq 0$ for $|\Theta| \gtrsim 10\,\mathrm{deg}$), and coplanar with respect to their common axis. If we introduce two Cartesian-like angular coordinates (α, β) centered on the common receivers axis, the visibilty would be written as the 2D Fourier transform of the product of the sky intensity and the receiver beam, for the angular frequency $(u, v)_{12} = (\frac{\Delta x}{\lambda}, \frac{\Delta y}{\lambda})$:

$$\mathcal{V}_{12}(\lambda) \simeq \iint \mathrm{d}\alpha\mathrm{d}\beta \ I(\alpha,\beta) \, L(\alpha,\beta) \exp\left[\mathrm{i}2\pi\left(\alpha\frac{\Delta x}{\lambda} + \beta\frac{\Delta y}{\lambda}\right)\right] \tag{17}$$

where $(\Delta x, \Delta y)$ are the two receiver distances on a plane perpendicular to the receiver axis. The x and y axes in the receiver plane are taken parallel to the two (α, β) angular planes. Furthermore, we introduce the conjugate Fourier variables (u, v) and the Fourier transforms of the sky intensity and the receiver beam:

$$(\alpha, \beta) \longrightarrow (u, v)$$
$$I(\alpha, \beta, \lambda) \longrightarrow \mathcal{I}(u, v, \lambda)$$
$$L(\alpha, \beta, \lambda) \longrightarrow \mathcal{L}(u, v, \lambda).$$

The visibility can then be interpreted as the weighted sum of the sky intensity, in an angular wave number domain located around $(u, v)_{12} = (\frac{\Delta x}{\lambda}, \frac{\Delta y}{\lambda})$. The weight function is given by the receiver-beam Fourier transform

$$\mathcal{V}_{12}(\lambda) \simeq \iint \mathrm{d}u\mathrm{d}v \ \mathcal{I}(u, v, \lambda) \, \mathcal{L}\left(u - \frac{\Delta x}{\lambda}, v - \frac{\Delta y}{\lambda}, \lambda\right). \tag{18}$$

A single receiver instrument would measure the total power integrated in a spot centered on the origin in the (u, v) or the angular wave-mode plane. The shape of the spot depends on the receiver
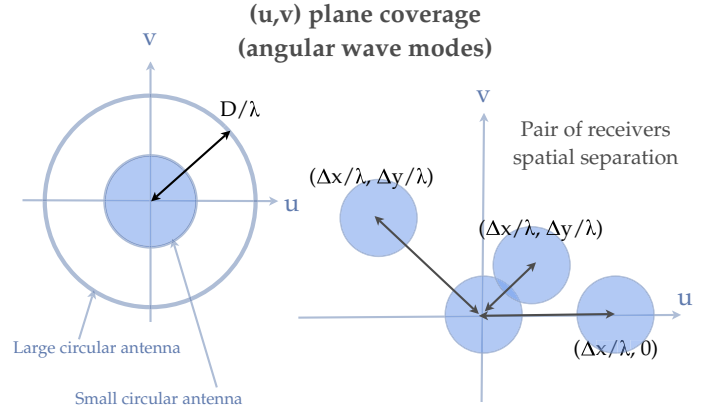
Fig. 2. Schematic view of the (u, v) plane coverage by interferometric measurement.

beam pattern, but its extent would be $\sim 2\pi D/\lambda$, where D is the receiver physical size.

The correlation signal from a pair of receivers would measure the integrated signal on a similar spot, located around the central angular wave-mode $(u, v)_{12}$, determined by the relative position of the two receivers (see Fig. 2). In an interferometer with multiple receivers, the area covered by different receiver pairs in the (u, v) plane might overlap, and some pairs might measure the same area (same base lines). Several beams can be formed using different combinations of the correlations from a set of antenna pairs.

An instrument can thus be characterized by its (u, v) plane coverage or response $\mathcal{R}(u, v, \lambda)$. For a single dish with a single receiver in the focal plane, the instrument response is simply the Fourier transform of the beam. For a single dish with multiple receivers, either as a focal plane array (FPA) or a multi-horn system, each beam (b) will have its own response $\mathcal{R}_b(u, v, \lambda)$. For an interferometer, we can compute a raw instrument response $\mathcal{R}_{\text{raw}}(u, v, \lambda)$, which corresponds to (u, v) plane coverage by all receiver pairs with uniform weighting. Obviously, different weighting schemes can be used, changing the effective beam shape, hence the response $\mathcal{R}_w(u, v, \lambda)$ and the noise behavior. If the same Fourier angular frequency mode is measured by several receiver pairs, the raw instrument response might then be larger that unity. This non-normalized instrument response is used to compute the projected noise power spectrum in the following Sect. (3.3). We can also define a normalized instrument response, $\mathcal{R}_{\text{norm}}(u, v, \lambda) \lesssim 1$ as

$$\mathcal{R}_{\text{norm}}(u, v, \lambda) = \mathcal{R}(u, v, \lambda)/\text{Max}_{(u, v)}\left[\mathcal{R}(u, v, \lambda)\right]. \tag{19}$$

This normalized instrument response is the basic ingredient for computing the effective instrument beam, in particular in Sect. 4.2.

Detection of the reionization at 21 cm has been an active field in the last decade, and different groups have built instruments to detect a reionization signal around 100 MHz: LOFAR (Rottering et al. 2006), MWA (Bowman et al. 2007; Lonsdale et al. 2009), and PAPER (Parsons et al. 2010). Several authors have studied the instrumental noise and statistical uncertainties when measuring the reionization signal power spectrum, and the methods presented here to compute the instrument response and sensitivities are similar to the ones developed in these publications (Morales & Hewitt 2004; Bowman et al. 2006; McQuinn et al. 2006).

3.2. Noise power spectrum computation

We consider a total power measurement using a receiver at wavelength λ, over a frequency bandwidth $\delta\nu$ centered on ν_0, with an integration time t_{int}, characterized by a system temperature T_{sys}. The uncertainty or fluctuations of this measurement due to the receiver noise can be written as $\sigma^2_{\mathrm{noise}} = \frac{2T^2_{\mathrm{sys}}}{t_{\mathrm{int}}\,\delta\nu}$. This term also corresponds to the noise for the visibility $\mathcal{V}_{12}$ measured from two identical receivers, with uncorrelated noise. If the receiver has an effective area $A \simeq \pi D^2/4$ or $A \simeq D_x D_y$, the measurement corresponds to the integration of power over a spot in the angular frequency plane with an area $\sim A/\lambda^2$. The noise's spectral density, in the angular frequency plane (per unit area of angular frequency $\delta u \times \delta v$), corresponding to a visibility measurement from a pair of receivers can be written as

$$P^{\mathrm{pair}}_{\mathrm{noise}} = \frac{\sigma^2_{\mathrm{noise}}}{A/\lambda^2} \qquad (20)$$

$$P^{\mathrm{pair}}_{\mathrm{noise}} \simeq \frac{2\,T^2_{\mathrm{sys}}}{t_{\mathrm{int}}\,\delta\nu}\frac{\lambda^2}{D^2} \qquad \text{units: } \mathrm{K}^2\,\mathrm{rad}^2. \qquad (21)$$

We can characterize the sky temperature measurement with a radio instrument by the noise's spectral power density in the angular frequencies plane $P_{\mathrm{noise}}(u, v)$ in units of Kelvin^2 per unit area of angular frequencies $\delta u \times \delta v$. For an interferometer made of identical receiver elements, several (n) receiver pairs might have the same baseline. The noise power density in the corresponding (u, v) plane area is then reduced by a factor $1/n$. More generally, we can write the instrument noise spectral power density using the instrument response defined in Sect. 3.1 as

$$P_{\mathrm{noise}}(u, v) = \frac{P^{\mathrm{pair}}_{\mathrm{noise}}}{\mathcal{R}_{raw}(u, v, \lambda)}. \qquad (22)$$

When the intensity maps are projected in a 3D box in the universe and the 3D power spectrum $P(k)$ is computed, angles are translated into comoving transverse distances, and frequencies or wavelengths into comoving radial distance, using the following relations (e.g. Chap. 13 of Peebles 1993; Rich 2001):

$$\alpha, \beta \rightarrow \ell_\perp = l_x, l_y = (1 + z)\,d_{\mathrm{A}}(z)\,\alpha, \beta \qquad (23)$$

$$u, v \rightarrow k_\perp = k_x, k_y = 2\pi \frac{u, v}{(1 + z)\,d_{\mathrm{A}}(z)} \qquad (24)$$

$$\delta\nu \rightarrow \delta\ell_\parallel = (1 + z)\frac{c}{H(z)}\frac{\delta\nu}{\nu} = (1 + z)\frac{\lambda}{H(z)}\delta\nu \qquad (25)$$

$$\frac{1}{\delta\nu} \rightarrow \delta k_\parallel = \delta k_z = 2\pi\frac{H(z)}{c}\frac{1}{(1 + z)}\frac{\nu}{\delta\nu} = \frac{H(z)}{c}\frac{1}{(1 + z)^2}\frac{\nu_{21}}{\delta\nu}. \qquad (26)$$

A brightness measurement at a point (u, v, λ), covering the 3D spot $(\delta u, \delta v, \delta\nu)$, would correspond to a cosmological power spectrum measurement at a transverse wave mode (k_x, k_y) defined by Eq. (24), measured at a redshift given by the observation frequency. The measurement noise spectral density given by Eq. (21) can then be translated into a 3D noise power spectrum, per unit of spatial frequencies $\delta k_x \times \delta k_y \times \delta k_z/8\pi^3$ (units: K^{2}Mpc^3):

$$(u, v, \lambda) \rightarrow k_x(u), k_y(v), z(\lambda) \qquad (27)$$

$$P_{\mathrm{noise}}(k_x, k_y, z) = P_{\mathrm{noise}}(u, v)\frac{8\pi^3 \delta u \times \delta v}{\delta k_x \times \delta k_y \times \delta k_z} \qquad (28)$$

$$= \left(2\frac{T^2_{\mathrm{sys}}}{t_{\mathrm{int}}\,\nu_{21}}\frac{\lambda^2}{D^2}\right)\frac{1}{\mathcal{R}_{\mathrm{raw}}}d^2_{\mathrm{A}}(z)\frac{c}{H(z)}(1 + z)^4. \qquad (29)$$

It is worthwhile to note that the "cosmological" 3D noise power spectrum does not depend anymore on the individual measurement bandwidth. In the following paragraph, we will first consider an ideal instrument with uniform (u, v) coverage in order to establish the general noise power spectrum behavior for cosmological 21 cm surveys. The numerical method used to compute the 3D noise power spectrum is then presented in Sect. 3.2.2.

3.2.1. Uniform (u, v) coverage

We consider here an instrument with uniform (u, v) plane coverage ($\mathcal{R}(u, v) = 1$), and measurements at regularly spaced frequencies centered on a central frequency ν_0 or redshift $z(\nu_0)$. The noise's spectral power density from Eq. (29) would then be constant, independent of $(k_x, k_y, \ell_\parallel(\nu))$. Such a noise power spectrum thus corresponds to a 3D white noise, with a uniform noise spectral density:

$$P_{\mathrm{noise}}(k_\perp, l_\parallel(\nu)) = P_{\mathrm{noise}} = 2\frac{T^2_{\mathrm{sys}}}{t_{\mathrm{int}}\,\nu_{21}}\frac{\lambda^2}{D^2}d^2_{\mathrm{A}}(z)\frac{c}{H(z)}(1 + z)^4 \quad (30)$$

where P_{noise} would be in units of mK^2 Mpc^3 with T_{sys} expressed in mK, t_{int} is the integration time expressed in second, ν_{21} in Hz, c in km s^{-1}, d_{A} in Mpc and $H(z)$ in km s^{-1} Mpc^{-1}.

The statistical uncertainties of matter or H$_{\mathrm{I}}$ distribution power spectrum estimate decreases with the number of observed Fourier modes, a number that is proportional to the volume of the universe being observed (sample variance). As the observed volume is proportional to the surveyed solid angle, we consider the survey of a fixed fraction of the sky, defined by total solid angle Ω_{tot}, performed during a given total observation time t_{obs}. A single-dish instrument with diameter D would have an instantaneous FOV $\Omega_{\mathrm{FOV}} \sim \left(\frac{\lambda}{D}\right)^2$, and would require a number of pointings $N_{\mathrm{point}} = \frac{\Omega_{\mathrm{tot}}}{\Omega_{\mathrm{FOV}}}$ to cover the survey area. Each sky direction or patch of size Ω_{FOV} will be observed during an integration time $t_{\mathrm{int}} = t_{\mathrm{obs}}/N_{\mathrm{point}}$. Using Eq. (30) and the previous expression for the integration time, we can compute a simple expression for the noise spectral power density by a single-dish instrument of diameter D:

$$P^{\mathrm{survey}}_{\mathrm{noise}}(k) = 2\frac{T^2_{\mathrm{sys}}\,\Omega_{\mathrm{tot}}}{t_{\mathrm{obs}}\,\nu_{21}}d^2_{\mathrm{A}}(z)\frac{c}{H(z)}(1 + z)^4. \qquad (31)$$

It is important to note that any real instrument does not have a flat response in the (u, v) plane, and the observations provide no information above a certain maximum angular frequency $u_{\mathrm{max}}, v_{\mathrm{max}}$. One has to take into account either a damping of the observed sky power spectrum or an increase in the noise spectral density if the observed power spectrum is corrected for damping. The white-noise expressions given below should thus be considered as a lower limit or floor of the instrument noise spectral density.

For a single-dish instrument of diameter D equipped with a multi-feed or phase-array receiver system, with N independent beams on sky, the noise spectral density decreases by a factor N, thanks to the increase in per pointing integration time:

$$P^{\mathrm{survey}}_{\mathrm{noise}}(k) = \frac{2}{N}\frac{T^2_{\mathrm{sys}}\,\Omega_{\mathrm{tot}}}{t_{\mathrm{obs}}\,\nu_{21}}d^2_{\mathrm{A}}(z)\frac{c}{H(z)}(1 + z)^4. \qquad (32)$$

This expression (Eq. (32)) can also be used for a filled interferometric array of N identical receivers with a total collection area $\sim D^2$. Such an array could be made for example of $N = q \times q$ small dishes, each with diameter D/q, arranged as a $q \times q$ square.
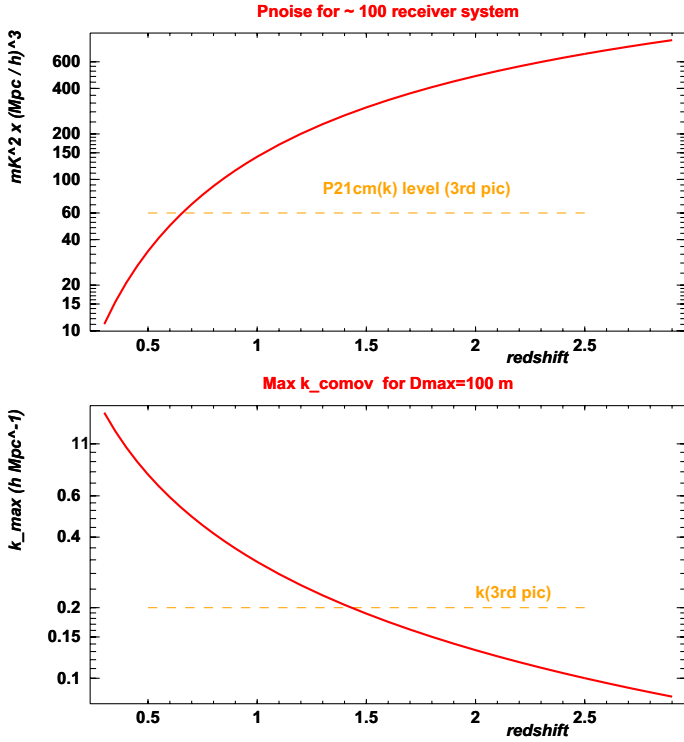
Fig. 3. *Top*: minimal noise level for a 100-beam instrument with $T_{sys} = 50$ K as a function of redshift (*top*), for a one-year survey of a quarter of the sky. *Bottom*: maximum k value for 21 cm LSS power spectrum measurement by a 100-m diameter primary antenna.

For a single dish of diameter D, or an interferometric instrument with maximal extent D, observations provide information up to $u_{max}, v_{max} \lesssim D/\lambda$. This value of u_{max}, v_{max} would be mapped to a maximum transverse cosmological wave number $k_\perp^{max}$:

$$k_\perp^{max} \lesssim \frac{2\pi}{d_A (1+z)^2} \frac{D}{\lambda_{21}}. \tag{33}$$

Figure 3 shows the evolution of the noise spectral density $P_{noise}^{survey}(k)$ as a function of redshift, for a radio survey of the sky, using an instrument with $N = 100$ beams and a system noise temperature $T_{sys} = 50$ K. The survey is supposed to cover a quarter of sky $\Omega_{tot} = \pi$ srad, in one year. The maximum comoving wave number k^{max} is also shown as a function of redshift, for an instrument with $D = 100$ m maximum extent. To take the radial component of $\boldsymbol{k}$ and the increase of the instrument noise level with $k_\perp$ into account, we have taken the effective k_{max} as half of the maximum transverse $k_\perp^{max}$ of Eq. (33):

$$k_{max}(z) = \frac{\pi}{d_A (1+z)^2} \frac{D = 100 \text{ m}}{\lambda_{21}}. \tag{34}$$

3.2.2. 3D noise power spectrum computation

We describe here the numerical method used to compute the 3D noise power spectrum, for a given instrument response, as presented in Sect. 3.3. The noise power spectrum is a good indicator to compare sensitivities for different instrument configurations, although the noise realization for a real instrument would not be isotropic.

– We start by a 3D Fourier coefficient grid, with the two first coordinates the transverse angular wave modes, and the third the frequency (k_x, k_y, ν). The grid is positioned at the mean redshift z_0 for which we want to compute $P_{noise}(k)$. For the results at redshift $z_0 = 1$ discussed in Sect. 3.3, the grid cell size and dimensions have been chosen to represent a box in the universe $\sim 1500 \times 1500 \times 750 \text{ Mpc}^3$, with $3 \times 3 \times 3 \text{ Mpc}^3$ cells. This corresponds to an angular wedge $\sim 25° \times 25° \times (\Delta z \simeq 0.3)$. Given the small angular extent, we have neglected the curvature of redshift shells.

– For each redshift shell $z(\nu)$, we compute a Gaussian noise realization. The coordinates (k_x, k_y) are converted to the (u, v) angular frequency coordinates using Eq. (24), and the angular diameter distance $d_A(z)$ for ΛCDM model with standard WMAP parameters (Komatsu et al. 2011). The noise variance is taken proportional to P_{noise}

$$\sigma_{re}^2 = \sigma_{im}^2 \propto \frac{1}{\mathcal{R}_{raw}(u, v, \lambda)} d_A^2(z) \frac{c}{H(z)} (1+z)^4. \tag{35}$$

– An FFT is then performed in the frequency or redshift direction to obtain the noise Fourier complex coefficients $\mathcal{F}_n(k_x, k_y, k_z)$ and the power spectrum is estimated as

$$\tilde{P}_{noise}(k) = \langle |\mathcal{F}_n(k_x, k_y, k_z)|^2 \rangle \text{ for } \sqrt{k_x^2 + k_y^2 + k_z^2} = k. \tag{36}$$

Noise samples corresponding to small instrument response, typically less than 1% of the maximum instrument response, are ignored when calculating $\tilde{P}_{noise}(k)$. However, we require a significant fraction, typically 20% to 50% of all possible modes (k_x, k_y, k_z) measured for a given k value.

– the above steps are repeated $\sim$50 times to decrease the statistical fluctuations from random generations. The averaged computed noise power spectrum is normalized using Eq. (29) and the instrument and survey parameters: system temperature $T_{sys} = 50$ K, individual receiver size D^2 or $D_x D_y$ and the integration time t_{int}. This last parameter is obtained through the relation $t_{int} = t_{obs} \Omega_{FOV}/\Omega_{tot}$ using the total survey duration $t_{obs} = 1$year, the instantaneous FOV $\Omega_{FOV} \sim \left(\frac{\lambda}{D}\right)^2$, and the total sky coverage $\Omega_{tot} = \pi$ srad.

It should be noted that it is possible to obtain a good approximation of the noise power spectrum shape by neglecting the redshift or frequency dependence of the instrument response function and $d_A(z)$ for a small redshift interval around z_0, using a fixed instrument response $\mathcal{R}(u, v, \lambda(z_0))$ and a constant radial distance $d_A(z_0) \times (1 + z_0)$:

$$\tilde{P}_{noise}(k) = \langle |\mathcal{F}_n(k_x, k_y, k_z)|^2 \rangle \simeq \langle P_{noise}(u, v, k_z) \rangle. \tag{37}$$

The approximate power spectrum obtained through this simplified and much faster method is shown as dashed curves in Fig. 6 for few instrument configurations.

3.3. Instrument configurations and noise power spectrum

We have numerically computed the instrument response $\mathcal{R}(u, v, \lambda)$ with uniform weights in the (u, v) plane for several instrument configurations:

a: A packed array of $n = 121$ $D_{dish} = 5$ m dishes, arranged in a square 11×11 configuration ($q = 11$). This array covers an area of $55 \times 55 \text{ m}^2$.
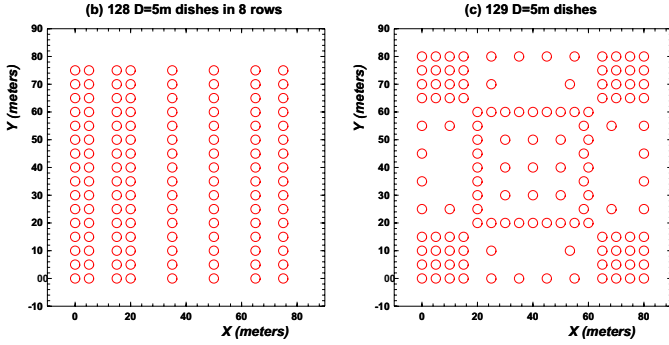
Fig. 4. Array layout for configurations **b)** and **c)** with 128 and 129 $D =$ 5 m diameter dishes.

b: An array of $n = 128 \, D_{\mathrm{dish}} = 5$ m dishes, arranged in eight rows, each with 16 dishes. These 128 dishes are spread over an area 80×80 m². The array layout for this configuration is shown in Fig. 4.

c: An array of $n = 129 \, D_{\mathrm{dish}} = 5$ m dishes, arranged over an area 80×80 m². This configuration has in particular four subarrays of packed 16 dishes (4×4), located in the four array corners. This array layout is also shown in Fig. 4.

d: A single-dish instrument, with diameter $D = 75$ m, equipped with a 100 beam focal plane receiver array.

e: A packed array of $n = 400 \, D_{\mathrm{dish}} = 5$ m dishes, arranged in a square 20×20 configuration ($q = 20$). This array covers an area of 100×100 m².

f: A packed array of four cylindrical reflectors, each 85 m long and 12 m wide. The focal line of each cylinder is equipped with 100 receivers, each 2λ long, corresponding to ~0.85 m at $z = 1$. This array covers an area of 48×85 m², and have a total of 400 receivers per polarization, as in the (e) configuration. We computed the noise power spectrum for *perfect* cylinders, where all receiver pair correlations are used (fp), or for an imperfect instrument, where only correlations between receivers from different cylinders are used.

g: A packed array of eight cylindrical reflectors, each 102 m long and 12 m wide. The focal line of each cylinder is equipped with 120 receivers, each 2λ long, corresponding to ~0.85 m at $z = 1$. This array covers an area of 96×102 m² and has a total of 960 receivers per polarization. As for the (f) configuration, we have computed the noise power spectrum for *perfect* cylinders, where all receiver pair correlations are used (gp), or for an imperfect instrument, where only correlations between receivers from different cylinders are used.

We used simple triangular shaped dish response in the (u, v) plane; however, we did introduce a filling factor or illumination efficiency η, relating the effective dish diameter D_{ill} to the mechanical dish size $D_{\mathrm{ill}} = \eta \, D_{\mathrm{dish}}$. The effective area $A_{\mathrm{e}} \propto \eta^2$ scales as η^2 or $\eta_x \eta_y$,

$$\mathcal{L}_\circ(u, v, \lambda) = \bigwedge_{[\pm\eta D_{\mathrm{dish}}/\lambda]} (\sqrt{u^2 + v^2}) \tag{38}$$

$$L_\circ(\alpha, \beta, \lambda) = \left[\frac{\sin(\pi(D^{\mathrm{ill}}/\lambda)\sin\theta)}{\pi(D^{\mathrm{ill}}/\lambda)\sin\theta} \right]^2 \quad \theta = \sqrt{\alpha^2 + \beta^2}. \tag{39}$$

For the multidish configuration studied here, we have taken the illumination efficiency factor $\eta = 0.9$.

For the receivers along the focal line of cylinders, we assumed that the individual receiver response in the (u, v) plane corresponds to a rectangular antenna. The illumination efficiency

factor was taken equal to $\eta_x = 0.9$ in the direction of the cylinder width, and $\eta_y = 0.8$ along the cylinder length. We used a double triangular response function in the (u, v) plane for each of the receiver elements along the cylinder:

$$\mathcal{L}_\square(u, v, \lambda) = \bigwedge_{[\pm\eta_x D_x/\lambda]} (u) \times \bigwedge_{[\pm\eta_y D_y/\lambda]} (v). \tag{40}$$

It should be noted that the small angle approximation used here for the expression of visibilities is not valid for the receivers along the cylinder axis. However, some preliminary numerical checks indicate that the results for the noise spectral power density would not change significantly. The instrument responses shown here correspond to a fixed pointing toward the zenith, which is the case for a transit type telescope.

Figure 5 shows the instrument response $\mathcal{R}(u, v, \lambda)$ for the four configurations (a, b, c, d) with ~100 receivers per polarization. Using the numerical method sketched in Sect. 3.2.2, we computed the 3D noise power spectrum for each of the eight instrument configurations presented here, with a system noise temperature $T_{\mathrm{sys}} = 50$ K, for a one year survey of a quarter of sky $\Omega_{\mathrm{tot}} = \pi$ srad at a mean redshift $z_0 = 1$, $\nu_0 = 710$ MHz. The resulting noise spectral power densities are shown in Fig. 6. The increase of $P_{\mathrm{noise}}(k)$ at low $k^{\mathrm{comov}} \lesssim 0.02$ is due to our having ignored all auto-correlation measurements. It can be seen that an instrument with $100-200$ beams and $T_{\mathrm{sys}} = 50$ K should have enough sensitivity to map LSS in 21 cm at redshift $z = 1$.

4. Foregrounds and component separation

Reaching the required sensitivities is not the only difficulty of observing the LSS in 21 cm. Indeed, the synchrotron emission of the Milky Way and the extragalactic radio sources are a thousand times brighter than the emission of the neutral hydrogen distributed in the universe. Extracting the LSS signal using intensity mapping, without identifying the H_I point sources is the main challenge for this novel observation method. Although this task might seem impossible at first, it has been suggested that the smooth frequency dependence of the synchrotron emissions can be used to separate the faint LSS signal from the Galactic and radio source emissions. Discussion of contribution of different sources of radio foregrounds for measurement of reionization through redshifted 21 cm, as well as foreground subtraction using their smooth frequency dependence, can be found in (Shaver et al. 1999; Di Matteo et al. 2002; Oh & Mack 2003). However, any real radio instrument has a beam shape that changes with frequency, and this instrumental effect significantly increases the difficulty and complexity of this component separation technique. The effect of frequency dependent beam shape is sometimes referred to as *mode mixing*, and its impact on foreground subtraction has been discussed for example in Morales et al. (2006).

In this section, we present a short description of the foreground emissions and the simple models we used for computing the sky radio emissions in the GHz frequency range. We also present a simple component-separation method to extract the LSS signal and its performance. The analysis presented here follows a similar path to a detailed foreground subtraction study carried out for MWA at ~150 MHz by Bowman et al. (2009). We computed in particular, the effect of the instrument response on the recovered power spectrum. The results presented in this section concern the total sky emission and the LSS 21 cm signal extraction in the $z \sim 0.6$ redshift range, corresponding to the central frequency $\nu \sim 884$ MHz.
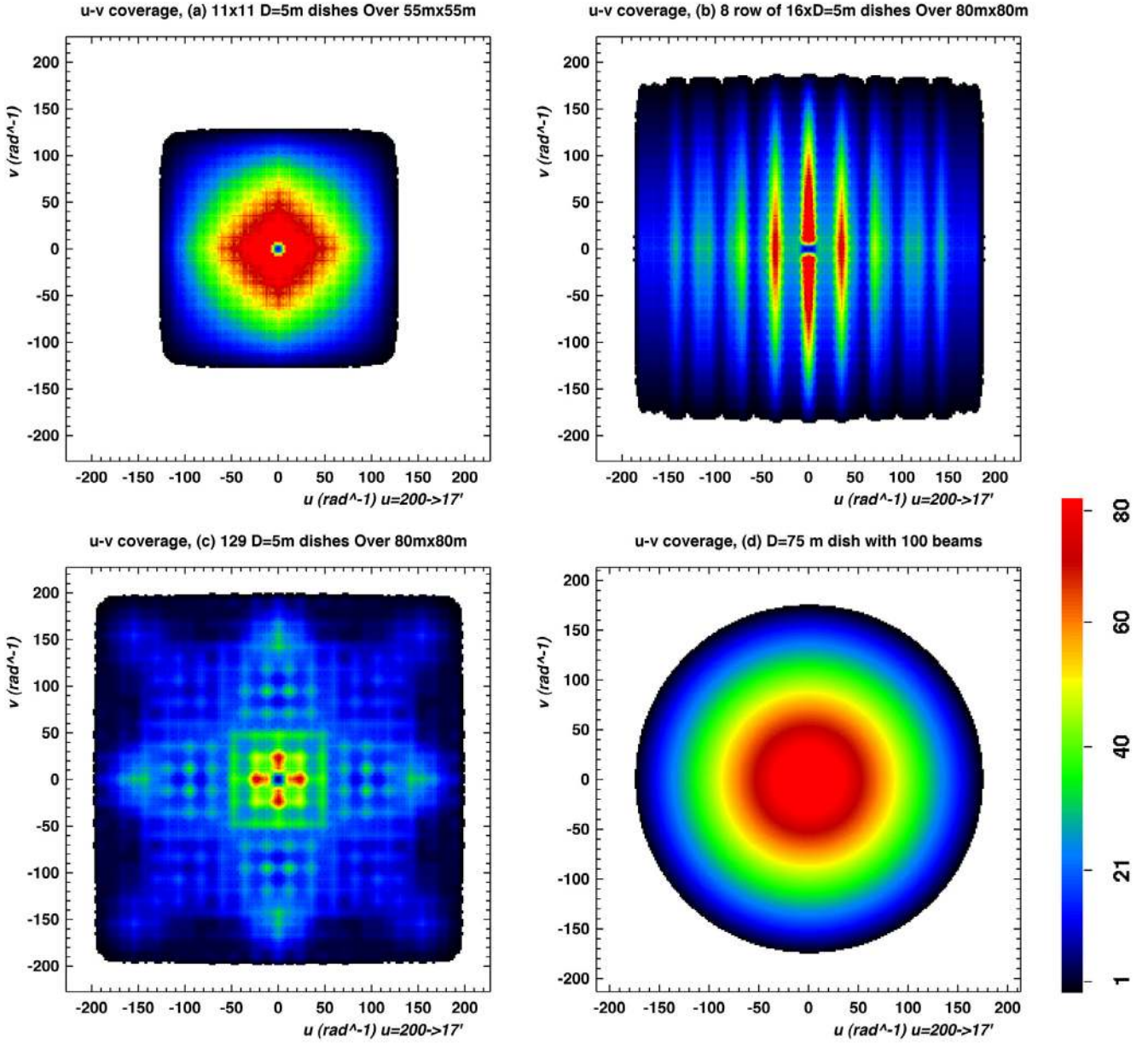
Fig. 5. Raw instrument response $\mathcal{R}_{raw}(u, v, \lambda)$ or the (u, v) plane coverage at 710 MHz (redshift $z = 1$) for four configurations. **a)** 121 $D_{dish} = 5$-m diameter dishes arranged in a compact, square array of 11×11, **b)** 128 dishes arranged in 8 rows of 16 dishes each (Fig. 4), **c)** 129 dishes arranged as shown in Fig. 4, **d)** single $D = 75$ meter diameter, with 100 beams. The common color scale (1 ... 80) is shown on the right.

4.1. Synchrotron and radio sources

We modeled the radio sky in the form of 3D maps (data cubes) of sky temperature brightness $T(\alpha, \delta, \nu)$ as a function of two equatorial angular coordinates (α, δ) and the frequency ν. Unless otherwise specified, the results presented here are based on simulations of $90 \times 30 \simeq 2500 \deg^2$ of the sky, centered on $\alpha = 10^h00^m, \delta = +10$ deg, and covering 128 MHz in frequency. We have selected this particular area of the sky in order to minimize the Galactic synchrotron foreground. The sky cube characteristics (coordinate range, size, resolution) used in the simulations are given in Table 3.

Two different methods were used to compute the sky temperature data cubes. We used the global sky model (GSM) (Oliveira-Costa et al. 2008) tools to generate full sky maps of the emission temperature at different frequencies, from which we extracted the brightness temperature cube for the region

defined above (Model-I/GSM $T_{gsm}(\alpha, \delta, \nu)$). Because the GSM maps have an intrinsic resolution of ~0.5 degree, it is difficult to have reliable results for the effect of point sources on the reconstructed LSS power spectrum.

We have thus also made a simple sky model using the Haslam Galactic synchrotron map at 408 MHz (Haslam et al. 1982) and the NRAO VLA Sky Survey (NVSS) 1.4 GHz radio source catalog (Condon et al. 1998). The sky temperature cube in this model (Model-II/Haslam+NVSS) was computed through the following steps:

1. The Galactic synchrotron emission is modeled as a power law with a spatially varying spectral index. We assign a power law index $\beta = -2.8 \pm 0.15$ to each sky direction, where β has a Gaussian distribution centered on –2.8 with a standard deviation $\sigma_\beta = 0.15$. The diffuse radio background spectral index has been measured, for example, by
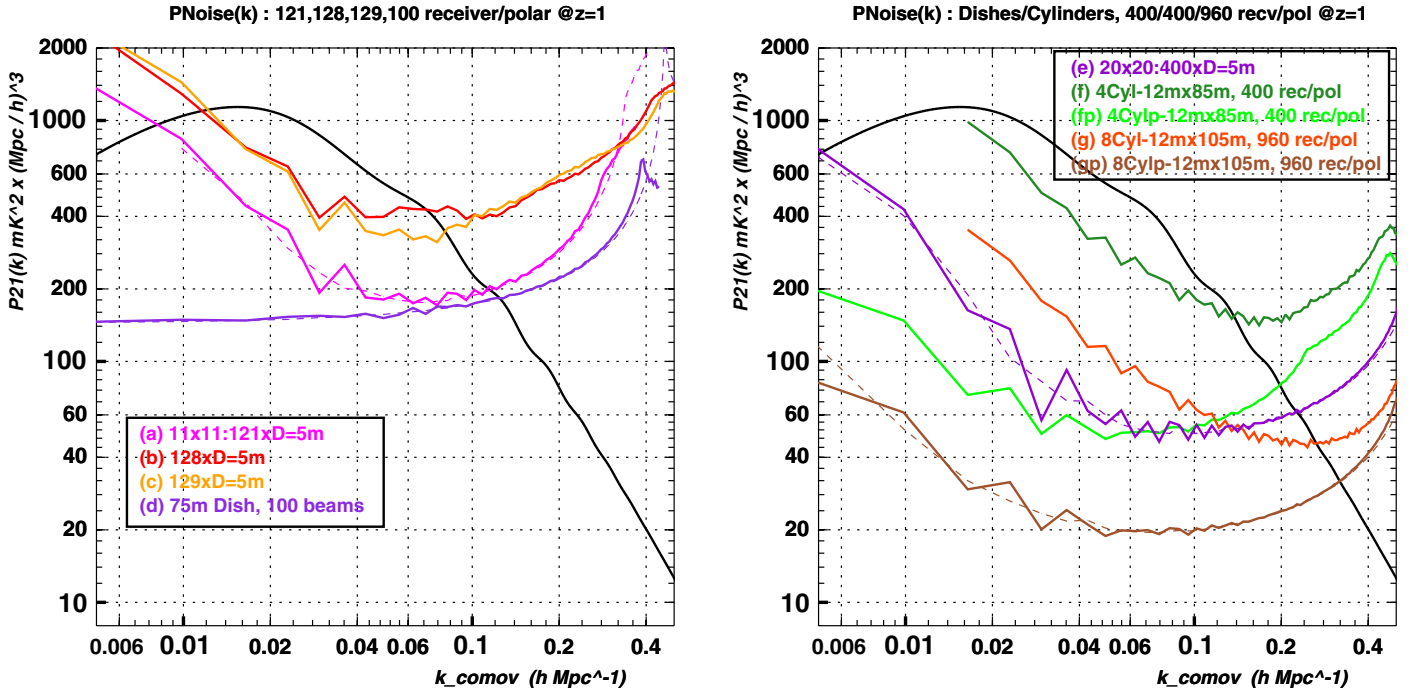
Fig. 6. $P(k)$ 21 cm LSS power spectrum at redshift $z = 1$ with $f_{H_I} = 2\%$ and the noise power spectrum for several interferometer configurations ((a), (b), (c), (d), (e), (f), (g)) with 121, 128, 129, 400, and 960 receivers. The noise power spectrum has been computed for all configurations assuming a survey of a quarter of the sky over one year, with a system temperature $T_{sys} = 50$ K.

Table 3. Sky cube characteristics for the simulations described in this paper.

	Range	Center
Right ascension	$105 < \alpha < 195$ deg	150 deg
Declination	$-5 < \delta < 25$ deg	+10 deg
Frequency	$820 < \nu < 948$ MHz	884 MHz
Wavelength	$36.6 < \lambda < 31.6$ cm	33.9 cm
Redshift	$0.73 < z < 0.5$	0.61
	resolution	N-cells
Right ascension	3 arcmin	1800
Declination	3 arcmin	600
Frequency	500 kHz (d$z \sim 10^{-3}$)	256

Notes. Cube size: $90 \deg \times 30 \deg \times 128$ MHz; $1800 \times 600 \times 256 \simeq 123 \times 10^6$ cells.

Platania et al. (1998) or Rogers & Bowman (2008). The synchrotron contribution to the sky temperature for each cell is then obtained through the formula:

$$T_{sync}(\alpha, \delta, \nu) = T_{haslam} \times \left(\frac{\nu}{408 \, \text{MHz}}\right)^{\beta}. \tag{41}$$

2. A 2D $T_{nvss}(\alpha, \delta)$ sky brightness temperature at 1.4 GHz is computed by projecting the radio sources in the NVSS catalog to a grid with the same angular resolution as the sky cubes. The source brightness in Jansky is converted to temperature taking the pixel angular size into account ($\sim$21mK/mJy at 1.4 GHz and $3' \times 3'$ pixels). A spectral index $\beta_{src} \in [-1.5, -2]$ is also assigned to each sky direction for the radio source map. We have taken β_{src} as a flat random number in the range $[-1.5, -2]$, and the contribution of the radiosources to the sky temperature is computed as:

$$T_{radsrc}(\alpha, \delta, \nu) = T_{nvss} \times \left(\frac{\nu}{1420 \, \text{MHz}}\right)^{\beta_{src}}. \tag{42}$$

3. The sky brightness temperature data cube is obtained through the sum of the two contributions, Galactic synchrotron and resolved radio sources:

$$T_{fgnd}(\alpha, \delta, \nu) = T_{sync}(\alpha, \delta, \nu) + T_{radsrc}(\alpha, \delta, \nu). \tag{43}$$

The 21 cm temperature fluctuations due to neutral hydrogen in LSS $T_{lss}(\alpha, \delta, \nu)$ were computed using the SimLSS[1] software package, where complex normal Gaussian fields were first generated in Fourier space. The amplitude of each mode was then multiplied by the square root of the power spectrum $P(k)$ at $z = 0$ computed according to the parametrization of Eisentein & Hu (1998). We used the standard cosmological parameters, $H_0 = 71$ km s^{-1} Mpc^{-1}, $\Omega_m = 0.264$, $\Omega_b = 0.045$, $\Omega_\lambda = 0.73$ and $w = -1$ (Komatsu et al. 2011). An inverse FFT was then performed to compute the matter density fluctuations $\delta\rho/\rho$ in the linear regime, in a box of $3420 \times 1140 \times 716$ Mpc^3, and evolved to redshift $z = 0.6$. The size of the box is about 2500 deg^2 in the transverse direction and $\Delta z \simeq 0.23$ in the longitudinal direction. The size of the cells is $1.9 \times 1.9 \times 2.8$ Mpc^3, which correspond approximately to the sky cube angular and frequency resolution defined above. We did not take the curvature of redshift shells into account when converting SimLSS Euclidean coordinates to angles and frequency coordinates of the sky cubes analyzed here. This approximate treatment causes distortions visible at large angles $\gtrsim 10°$. These angular scales correspond to small wave modes $k \lesssim 0.02 \, h$ Mpc^{-1} and are excluded for results presented in this paper.

The mass fluctuations have been converted into temperature using Eq. (10), and a neutral hydrogen fraction $0.008 \times (1 + 0.6)$, leading to a mean temperature of 0.13 mK. The total sky brightness temperature is computed as the sum of foregrounds and the LSS 21 cm emission:

$$T_{sky} = T_{sync} + T_{radsrc} + T_{lss} \quad \text{or} \quad T_{sky} = T_{gsm} + T_{lss}. \tag{44}$$

[1] SimLSS: http://www.sophya.org/SimLSS

Table 4. Mean temperature and standard deviation for different sky cubes.

	Mean (K)	Std. dev (K)
Haslam	2.17	0.6
NVSS	0.13	7.73
Haslam+NVSS	2.3	7.75
(Haslam+NVSS)*Lobe(35′)	2.3	0.72
GSM	2.1	0.8

Table 4 summarizes the mean and standard deviation of the sky brightness temperature $T(\alpha, \delta, \nu)$ for the different components computed in this study. It should be noted that the standard deviation depends on the map resolution, and the values given in Table 4 correspond to sky cubes computed here, with ~3 arcmin angular and 500 kHz frequency resolutions (see Table 3). Figure 8 shows the comparison of the GSM temperature map at 884 MHz with Haslam+NVSS map, smoothed with a 35 arcmin Gaussian beam. Figure 7 shows the comparison of the sky cube temperature distribution for Model-I/GSM and Model-II. There is good agreement between the two models, although the mean temperature for Model-II is slightly higher (~10%) than Model-I.

We computed the power spectrum for the 21 cm-LSS sky temperature cube, as well as for the radio foreground temperature cubes obtained from the two models. We also computed the power spectrum on sky brightness temperature cubes, as measured by a perfect instrument having a 25 arcmin (FWHM) Gaussian beam. The resulting computed power spectra are shown in Fig. 9. The GSM model has more large-scale power compared to our simple Haslam+NVSS model, while it lacks power at higher spatial frequencies. The mode mixing due to a frequency-dependent response will thus be stronger in Model-II (Haslam+NVSS) case. It can also be seen that the radio foreground's power spectrum is more than ~10^6 times higher than the 21 cm signal from LSS. This corresponds to the factor ~10^3 of the sky brightness temperature fluctuations (~K), compared to the mK LSS signal.

In contrast to most similar studies, where it is assumed that bright sources can be nearly perfectly subtracted, our aim was to compute also their effect in the foreground subtraction process. The GSM model lacks the angular resolution needed to correctly compute the effect of bright compact sources for 21 cm LSS observations and the mode mixing due to the frequency dependence of the instrumental response, while Model-II provides a reasonable description of these compact sources. Our simulated sky cubes have an angular resolution $3′ \times 3′$, well below the typical 15′ resolution of the instrument configuration considered here. However, Model-II might lack spatial structures on large scales, above a degree, compared to Model-I/GSM, and the frequency variations as a simple power law might not be realistic enough. The differences for the two sky models can be seen in their power spectra shown in Fig. 9. The smoothing or convolution with a 25′ beam has negligible effect on the GSM power spectrum, since it originally lacks structures below 0.5 degree. By using these two models, we explored some of the systematic uncertainties related to foreground subtraction.

It should also be noted that in Sect. 3, we presented the different instrument configuration noise levels after *correcting or deconvolving* the instrument response. The LSS power spectrum is recovered unaffected in this case, while the noise power spectrum increases at high k values (small scales). In practice, clean deconvolution is difficult to implement for real data
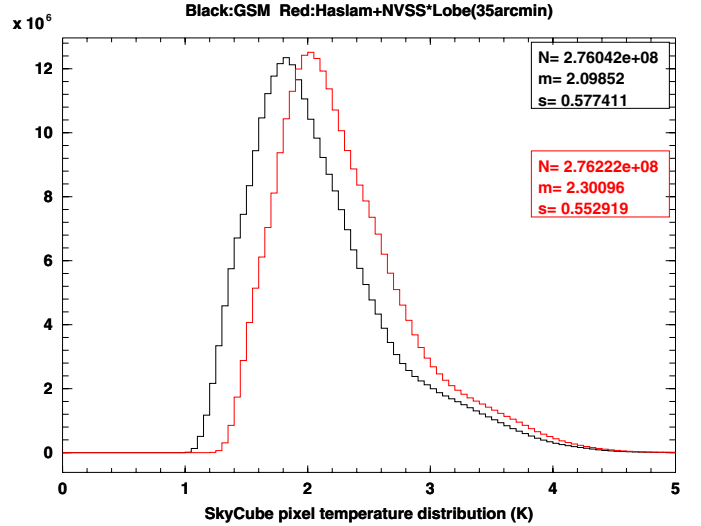
Fig. 7. Comparison of GSM (black) and Model-II (red) sky cube temperature distribution. The Model-II (Haslam+NVSS), has been smoothed with a 35 arcmin Gaussian beam.

and the power spectra presented in this section are NOT corrected for the instrumental response. The observed structures thus have a scale-dependent damping according to the instrument response, while the instrument noise is flat (white noise or scale-independent).

4.2. Instrument response and LSS signal extraction

The *observed* data cube is obtained from the sky brightness temperature 3D map $T_{sky}(\alpha, \delta, \nu)$ by applying the frequency or wavelength dependent instrument response $\mathcal{R}(u, v, \lambda)$. We have considered the simple case where the instrument response is constant throughout the survey area, or independent of the sky direction. For each frequency ν_k or wavelength $\lambda_k = c/\nu_k$:

1. Apply a 2D Fourier transform to compute sky angular Fourier amplitudes

   $$T_{sky}(\alpha, \delta, \lambda_k) \rightarrow 2D-FFT \rightarrow \mathcal{T}_{sky}(u, v, \lambda_k).$$

2. Apply instrument response in the angular wave mode plane. We use here the normalized instrument response $\mathcal{R}(u, v, \lambda_k) \lesssim 1$

   $$\mathcal{T}_{sky}(u, v, \lambda_k) \longrightarrow \mathcal{T}_{sky}(u, v, \lambda_k) \times \mathcal{R}(u, v, \lambda_k).$$

3. Apply inverse 2D Fourier transform to compute the measured sky brightness temperature map without instrumental (electronic/T_{sys}) white noise:

   $$\mathcal{T}_{sky}(u, v, \lambda_k) \times \mathcal{R}(u, v, \lambda) \rightarrow Inv-2D-FFT \rightarrow T_{mes1}(\alpha, \delta, \lambda_k).$$

4. Add white noise (Gaussian fluctuations) to the pixel map temperatures to obtain the measured sky brightness temperature $T_{mes}(\alpha, \delta, \nu_k)$. The white noise hypothesis is reasonable at this level, since (u, v) dependent instrumental response has already been applied. We also considered that the system temperature, and thus the additive white noise level, was independent of the frequency or wavelength.

The LSS signal extraction performance obviously depends on the white noise level. The results shown here correspond to the (a) instrument configuration, a packed array
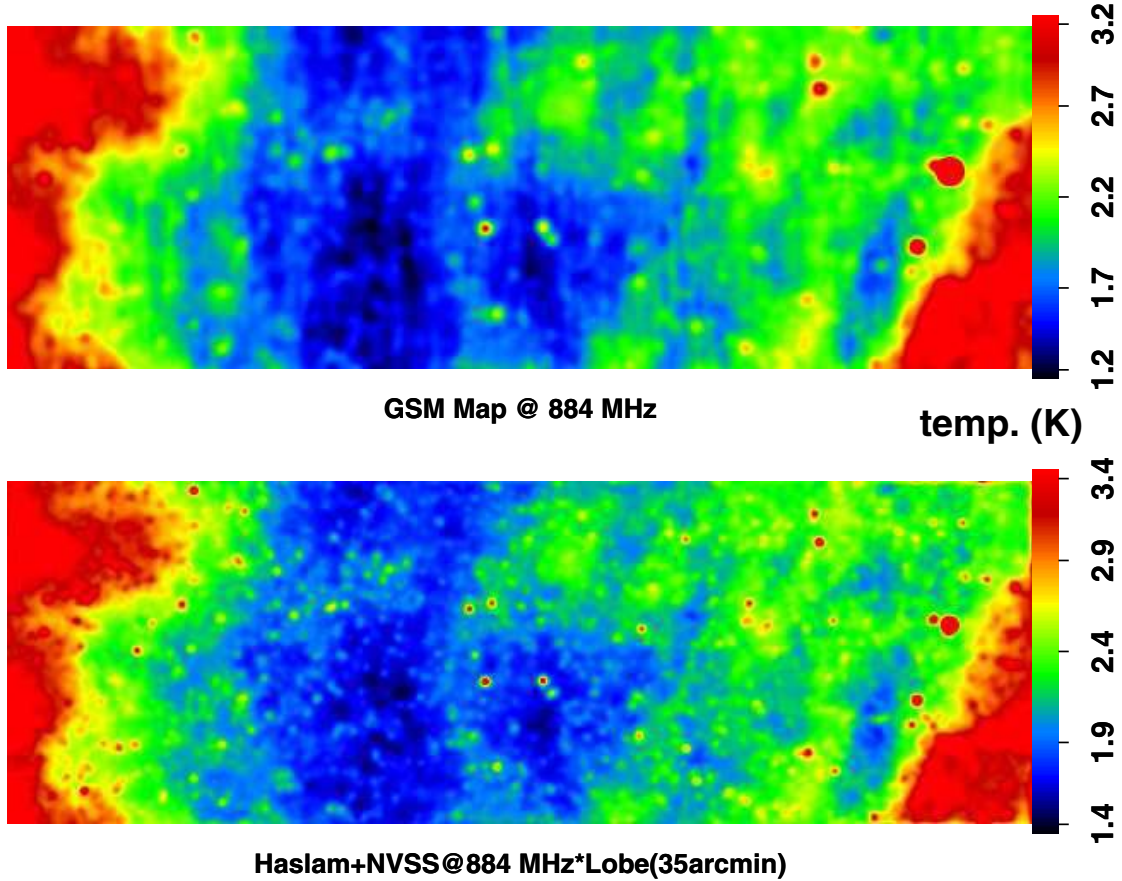
GSM Map @ 884 MHz

temp. (K)

Haslam+NVSS@884 MHz*Lobe(35arcmin)

Fig. 8. Comparison of GSM (*top*) and Model-II (*bottom*) sky maps at 884 MHz. The Model-II (Haslam+NVSS) has been smoothed with a 35 arcmin (FWHM) Gaussian beam.

of $11 \times 11 = 121$ dishes (5 m diameter), with a white noise level corresponding to $\sigma_{\text{noise}} = 0.25$ mK per 3×3 arcmin$^2 \times 500$ kHz cell.

The different steps in the simple component separation procedure that has been applied are briefly described here.

1. The measured sky brightness temperature is first *corrected* for the frequency dependent beam effects through a convolution by a fiducial frequency independent beam $\mathcal{R}_f(u, v)$ This *correction* corresponds to a smearing or degradation of the angular resolution

$$\mathcal{T}_{\text{mes}}(u, v, \lambda_k) \rightarrow \mathcal{T}_{\text{mes}}^{\text{bcor}}(u, v, \lambda_k)$$

$$\mathcal{T}_{\text{mes}}^{\text{bcor}}(u, v, \lambda_k) = \mathcal{T}_{\text{mes}}(u, v, \lambda_k) \times \sqrt{\frac{\mathcal{R}_f(u, v)}{\mathcal{R}(u, v, \lambda)}}$$

$$\mathcal{T}_{\text{mes}}^{\text{bcor}}(u, v, \lambda_k) \rightarrow 2\text{D} - \text{FFT} \rightarrow T_{\text{mes}}^{\text{bcor}}(\alpha, \delta, \lambda).$$

The virtual target beam $\mathcal{R}_f(u, v)$ has a lower resolution than the worst real instrument beam, i.e. at the lowest observed frequency. No correction has been applied for modes with $\mathcal{R}(u, v, \lambda) \lesssim 1\%$, as a first attempt to represent imperfect knowledge of the instrument response. We recall that this is the normalized instrument response, $\mathcal{R}(u, v, \lambda) \lesssim 1$. The correction factor $\mathcal{R}_f(u, v)/\mathcal{R}(u, v, \lambda)$ also has a numerical upper bound ~100.

2. For each sky direction (α, δ), a power law $T = T_0 \left(\frac{\nu}{\nu_0}\right)^b$ is fitted to the beam-corrected brightness temperature. The parameters were obtained using a linear χ^2 fit in the

$\log_{10}(T), \log_{10}(\nu)$ plane. We show here the results for a pure power law (P1), as well as a modified power law (P2):

$$P1 : \log_{10}(T_{\text{mes}}^{\text{bcor}}(\nu)) = a + b \log_{10}(\nu/\nu_0)$$

$$P2 : \log_{10}(T_{\text{mes}}^{\text{bcor}}(\nu)) = a + b \log_{10}(\nu/\nu_0) + c \log_{10}(\nu/\nu_0)^2$$

where b is the power law index and $T_0 = 10^a$ the brightness temperature at the reference frequency ν_0.

Interferometers have a poor response at small (u, v) corresponding to baselines smaller than interferometer element size. The zero-spacing baseline, the $(u, v) = (0, 0)$ mode, represents the mean temperature for a given frequency plane and cannot be measured with interferometers. We used a simple trick to make the power-law fitting procedure applicable, by setting the mean value of the temperature for each frequency plane according to a power law with an index close to the synchrotron index ($\beta \sim -2.8$). And we checked that the results are not too sensitive to the arbitrarily fixed mean temperature power law parameters.

3. The difference between the beam-corrected sky temperature and the fitted power law $(T_0(\alpha, \delta), b(\alpha, \delta))$ is our extracted 21 cm LSS signal.

Figure 10 shows the performance of this procedure at a redshift ~0.6, for the two radio sky models used here: GSM/Model-I and Haslam+NVSS/Model-II. The 21 cm LSS power spectrum, as seen by a perfect instrument with a 25 arcmin (FWHM) Gaussian frequency independent beam is shown, as well as the extracted power spectrum, after beam *correction* and foreground separation with second order polynomial fit (P2). We have also
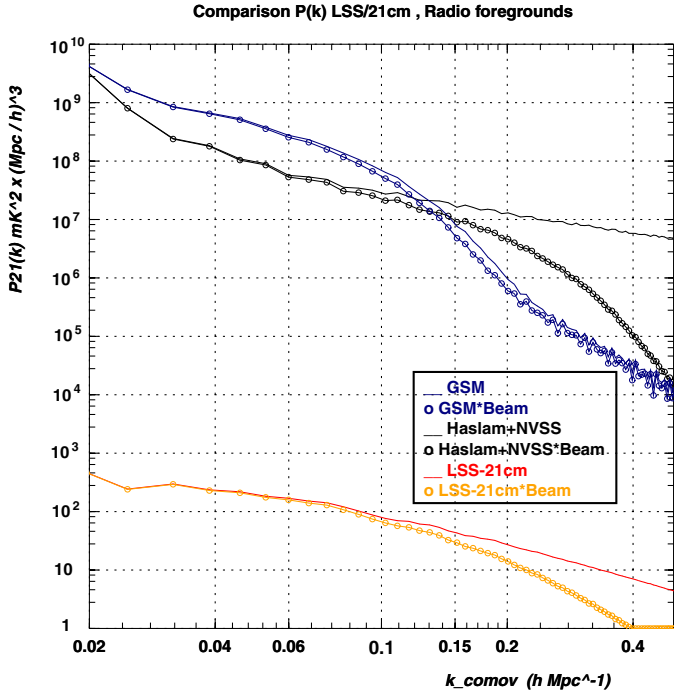
Fig. 9. Comparison of the 21 cm LSS power spectrum at $z = 0.6$ with $f_{\mathrm{H_I}} \simeq 1.3\%$ (red, orange) with the radio foreground power spectrum. The radio sky power spectrum is shown for the GSM (Model-I) sky model (dark blue), as well as for our simple model based on Haslam+NVSS (Model-II, black). The curves with circle markers show the power spectrum as observed by a perfect instrument with a 25 arcmin (FWHM) Gaussian beam.

represented the obtained power spectrum without applying the beam correction (step 1 above), or with the first-order polynomial fit (P1).

Figure 11 shows a comparison of the original 21 cm brightness temperature map at 884 MHz with the recovered 21 cm map, after subtracting the radio continuum component. It can be seen that structures present in the original map have been correctly recovered, although the amplitude of the temperature fluctuations on the recovered map is significantly smaller (factor ~5) than in the original map. This is mostly due to the damping of the large-scale power ($k \lesssim 0.1\,h\,\mathrm{Mpc}^{-1}$) due to the foreground subtraction procedure (see Fig. 12).

We have shown that it should be possible to measure the redshifted 21 cm emission fluctuations in the presence of the strong radio continuum signal, provided that the latter has a smooth frequency dependence. However, a rather precise knowledge of the instrument beam and the beam *correction* or smearing procedure described here are key ingredients for recovering the 21 cm LSS power spectrum. It is also important to note that, while it is enough to correct the beam to the lowest resolution instrument beam (~30′ or $D \sim 50$ m @ 820 MHz) for the GSM sky model, a stronger beam correction has to be applied (~36′ or $D \sim 40$ m @ 820 MHz) for Model-II to reduce significantly the ripples from bright radio sources. We have also applied the same procedure to simulate observations and LSS signal extraction for an instrument with a frequency-dependent Gaussian beam shape. The mode mixing effect is greatly reduced for such a smooth beam, compared to the more complex instrument response $\mathcal{R}(u, v, \lambda)$ used for the results shown in Fig. 10.

4.3. $P_{21}(k)$ measurement transfer function

The recovered red shifted 21 cm emission power spectrum $P_{21}^{\mathrm{rec}}(k)$ suffers a number of distortions, mostly damping, compared to the original $P_{21}(k)$ due to the instrument response and the component separation procedure. We recall that we have neglected the curvature of redshift or frequency shells in this numerical study, which affect our result at large angles $\gtrsim 10°$. The results presented here and our conclusions are thus restricted to the wave-mode range $k \gtrsim 0.02\,h\,\mathrm{Mpc}^{-1}$. We expect damping on small scales, or large k, due to the finite instrument size, but also on large scales, small k, if total power measurements (auto-correlations) are not used in the case of interferometers. The sky reconstruction and the component separation introduce additional filtering and distortions. The real transverse plane transfer function might even be anisotropic.

However, within the scope of the present study, we define an overall transfer function $\mathbf{T}(k)$ as the ratio of the recovered 3D power spectrum $P_{21}^{\mathrm{rec}}(k)$ to the original $P_{21}(k)$, similar to the one defined by Bowman et al. (2009), Eq. (23):

$$\mathbf{T}(k) = P_{21}^{\mathrm{rec}}(k)/P_{21}(k). \tag{45}$$

Figure 12 shows this overall transfer function for the simulations and component separation performed here, around $z \sim 0.6$, for the instrumental setup (a), a filled array of 121 $D_{\mathrm{dish}} = 5$ m dishes. This transfer function has been obtained after averaging the reconstructed $P_{21}^{\mathrm{rec}}(k)$ for several realizations (50) of the LSS temperature field. The black curve shows the ratio $\mathbf{T}(k) = P_{21}^{\mathrm{beam}}(k)/P_{21}(k)$ of the computed to the original power spectrum, if the original LSS temperature cube is smoothed by the frequency independent target beam $FWHM = 30'$. This black curve shows the damping effect due to the finite instrument size at small scales ($k \gtrsim 0.1\,h\,\mathrm{Mpc}^{-1}, \theta \lesssim 1°$). The transfer function for the GSM foreground model (Model-I) and the 11×11 filled array interferometer (setup (a)) is represented, as well as the transfer function for a $D = 55$ m diameter dish. The transfer function for the Model-II/Haslam+NVSS and the setup (a) filled interferometer array is also shown. The recovered power spectrum also suffers significant damping on large scales $k \lesssim 0.05\,h\,\mathrm{Mpc}^{-1}$, mostly due to the filtering of radial or longitudinal Fourier modes along the frequency or redshift direction ($k_\parallel$) by the component separation algorithm. We were able to remove the ripples on the reconstructed power spectrum due to bright sources in the Model-II by applying a stronger beam correction, ~36′ target beam resolution, compared to ~30′ for the GSM model. This explains the lower transfer function obtained for Model-II on small scales ($k \gtrsim 0.1\,h\,\mathrm{Mpc}^{-1}$).

It should be stressed that the simulations presented in this section were focused on the study of the radio foreground effects and have been carried intentionally with a very low instrumental noise level of 0.25 mK per pixel, corresponding to several years of continuous observations (~10 h per 3′×3′ pixel). This transfer function is well represented by the analytical form:

$$\mathbf{T}(k) = \sqrt{\frac{k - k_{\mathrm{A}}}{k_{\mathrm{B}}}} \times \exp\left(-\frac{k}{k_{\mathrm{C}}}\right). \tag{46}$$

We simulated observations and radio foreground subtraction using the procedure described here for different redshifts and instrument configurations, in particular for the (e) configuration with 400 five-meter dishes. As the synchrotron and radio source strength increases quickly with decreasing frequency, we have seen that recovering the 21 cm LSS signal becomes difficult for higher redshifts, in particular for $z \gtrsim 2$.
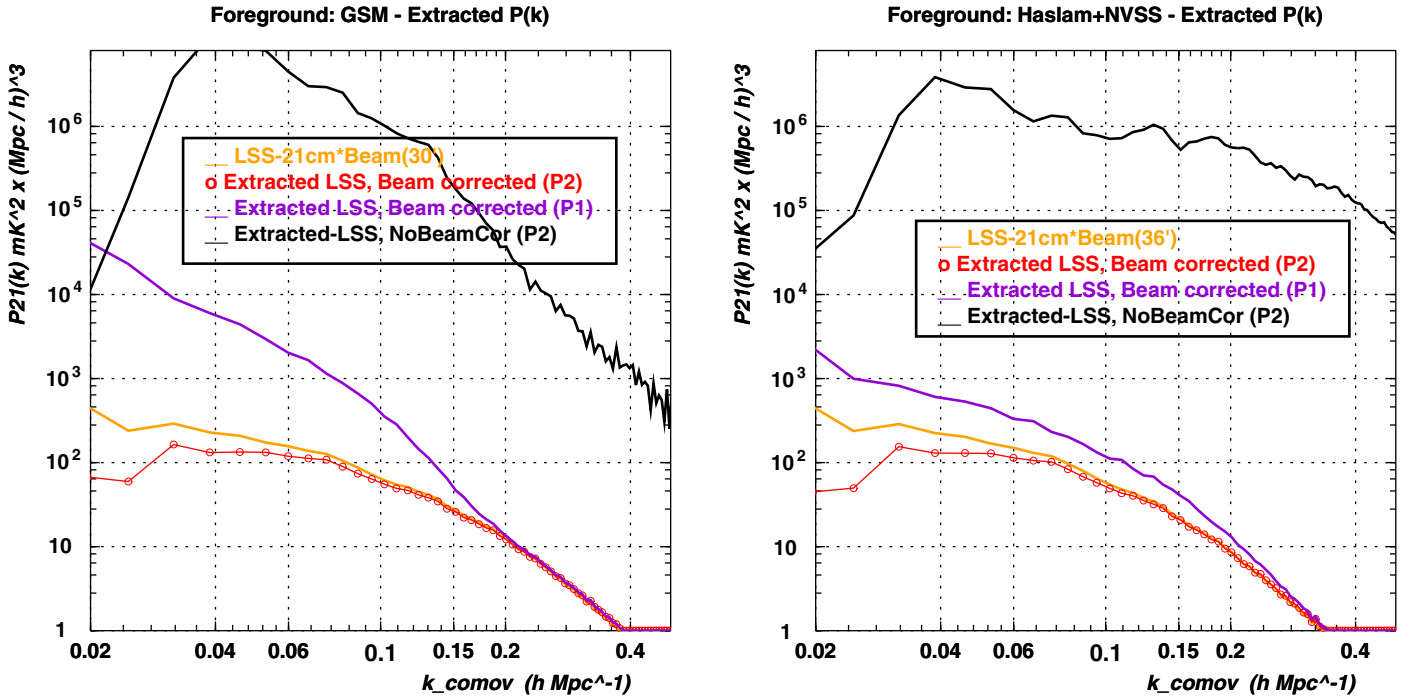
Foreground: GSM - Extracted P(k)

Foreground: Haslam+NVSS - Extracted P(k)

Fig. 10. Recovered power spectrum of the 21 cm LSS temperature fluctuations, separated from the continuum radio emissions at $z \sim 0.6$, $f_{H_I} \simeq 1.3\%$, for the instrument configuration (a), 11×11 packed array interferometer. *Left*: GSM/Model-I, *right*: Haslam+NVSS/Model-II. The black curve shows the residual after foreground subtraction, corresponding to the 21 cm signal, WITHOUT applying the beam correction. The red curve shows the recovered 21 cm signal power spectrum, for P2 type fit of the frequency dependence of the radio continuum, and violet curve is the P1 fit (see text). The orange curve shows the original 21 cm signal power spectrum, smoothed with a perfect, frequency-independent Gaussian beam.

Table 5. Transfer function parameters.

z	0.5	1.0	1.5	2.0	2.5
k_A (Mpc^{-1})	0.006	0.005	0.004	0.0035	0.003
k_B (Mpc^{-1})	0.038	0.019	0.012	0.0093	0.008
k_C (Mpc^{-1})	0.16	0.08	0.05	0.038	0.032

Notes. The transfer function parameters, (k_A, k_B, k_C) (Eq. (46)) at different redshifts and for instrumental setup (e), 20×20 packed array interferometer, are given in Mpc^{-1} unit, and not in h Mpc^{-1}.

We have determined the transfer function parameters of Eq. (46) k_A, k_B, k_C for setup (e) for three redshifts, $z = 0.5, 1, 1.5$, and then extrapolated the value of the parameters for redshift $z = 2, 2.5$. The value of the parameters are grouped in Table 5, and the corresponding transfer functions are shown in Fig. 13.

5. Sensitivity to cosmological parameters

The impact of the various telescope configurations on the sensitivity for 21 cm power spectrum measurement has been discussed in Sect. 3. Figure 6 shows the noise power spectra and allows us to visually rank the configurations in terms of instrument noise contribution to $P(k)$ measurement. The differences in P_{noise} will translate into differing precisions in the reconstruction of the BAO peak positions and in the estimation of cosmological parameters. In addition, we have seen (Sect. 4.2) that subtraction of continuum radio emissions, Galactic synchrotron, and radio sources also has an effect on the measured 21 cm power spectrum. In this paragraph, we present our method and the results for the precisions on the estimation of dark energy parameters through a radio survey of the redshifted 21 cm emission of

LSS, with an instrumental setup similar to the (e) configuration (Sect. 3.3), 400 five-meter diameter dishes, arranged into a filled 20×20 array.

5.1. BAO peak precision

To estimate the precision with which BAO peak positions can be measured, we used a method similar to the one established in (Blake & Glazebrook 2003) and (Glazebrook & Blake 2005). To this end, we generated reconstructed power spectra $P^{rec}(k)$ for slices of the Universe with a quarter-sky coverage and a redshift depth, $\Delta z = 0.5$ for $0.25 < z < 2.75$. The peaks in the generated spectra were then determined by a fitting procedure and the reconstructed peak positions compared with the generated peak positions. The reconstructed power spectrum used in the simulation is the sum of the expected H$_I$ signal term, corresponding to Eqs. (9) and (10), damped by the transfer function $\mathbf{T}(k)$ (Eq. (46), Table 5) and a white noise component P_{noise} calculated according to Eq. (32), established in Sect. 3.3 with $N = 400$:

$$P^{rec}(k) = P_{21}(k) \times \mathbf{T}(k) + P_{noise} \qquad (47)$$

where the different terms $(P_{21}(k), \mathbf{T}(k), P_{noise})$ depend on the slice redshift. The expected 21 cm power spectrum $P_{21}(k)$ has been generated according to the formula

$$\frac{P_{21}(k_\perp, k_\parallel)}{P_{ref}(k_\perp, k_\parallel)} = 1 + A\,k\,\exp(-(k/\tau)^\alpha)\sin\left(2\pi\sqrt{\frac{k_\perp^2}{k_{BAO\perp}^2} + \frac{k_\parallel^2}{k_{BAO\parallel}^2}}\right) \qquad (48)$$

where $k = \sqrt{k_\perp^2 + k_\parallel^2}$, the parameters A, α, and τ are adjusted to the formula presented in (Eisenstein & Hu 1998), and
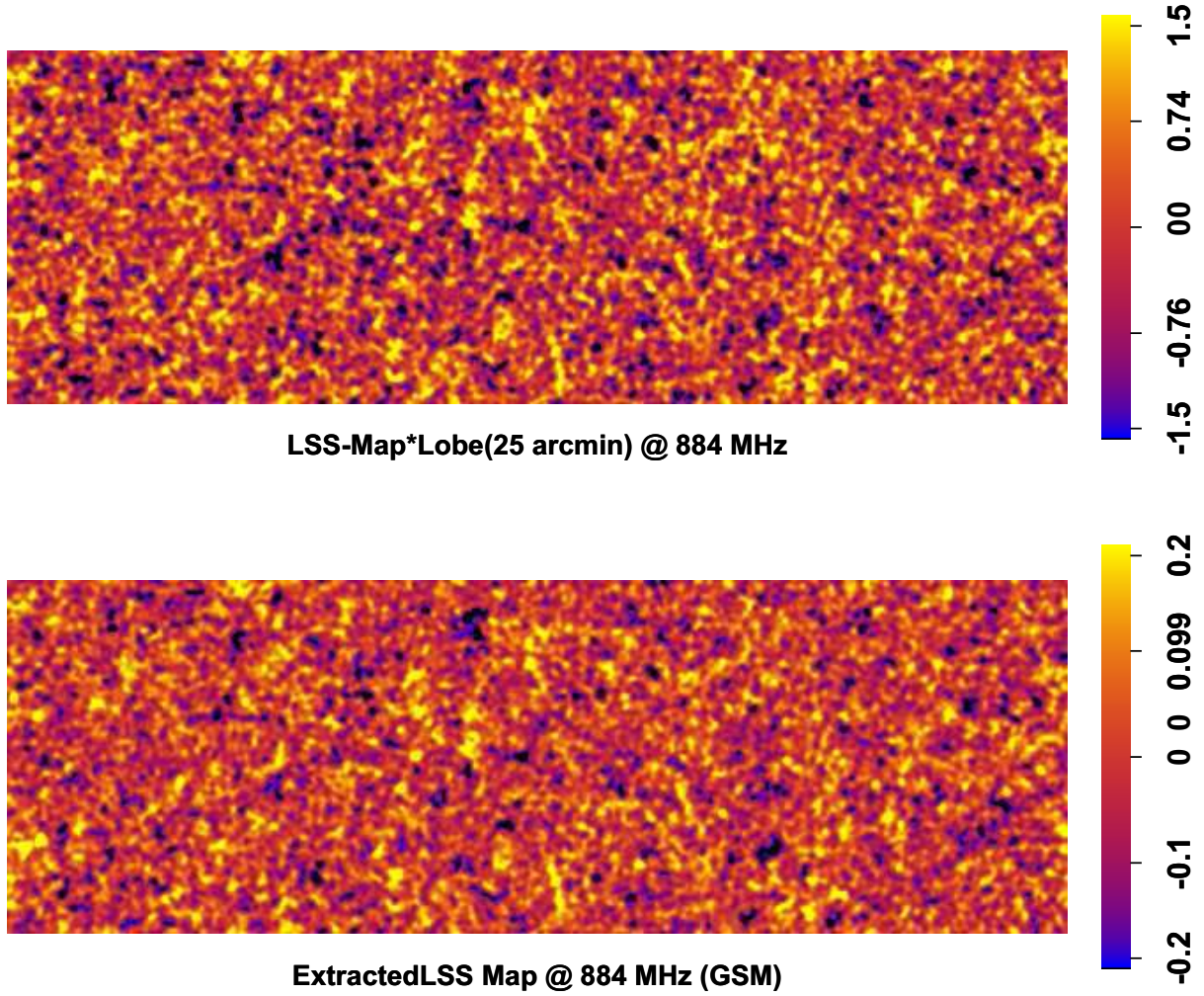
Fig. 11. Comparison of the original 21 cm LSS temperature map @ 884 MHz ($z \sim 0.6$), smoothed with 25 arcmin (FWHM) beam (*top*), and the recovered LSS map, after foreground subtraction for Model-I (GSM) (*bottom*), for the instrument configuration (a), 11×11 packed array interferometer.

$P_{\text{ref}}(k_\perp, k_\parallel)$ is the envelope curve of the HI power spectrum without baryonic oscillations. The parameters $k_{\text{BAO}\perp}$ and $k_{\text{BAO}\parallel}$ are the inverses of the oscillation periods in k-space. The following values were used for these parameters for the results presented here: $A = 1.0$, $\tau = 0.1\, h\,\text{Mpc}^{-1}$, $\alpha = 1.4$, and $k_{\text{BAO}\perp} = k_{\text{BAO}\parallel} = 0.060\, h\,\text{Mpc}^{-1}$.

Each simulation is performed for a given set of parameters: the system temperature T_{sys}, an observation time t_{obs}, an average redshift, and a redshift depth $\Delta z = 0.5$. Then, each simulated power spectrum is fitted with a 2D normalized function $P_{\text{tot}}(k_\perp, k_\parallel)/P_{\text{ref}}(k_\perp, k_\parallel)$, which is the sum of the signal power spectrum damped by the transfer function and the noise power spectrum multiplied by a linear term, $a_0 + a_1 k$. The upper limit k_{max} in k of the fit corresponds to the approximate position of the linear/nonlinear transition. This limit is established on the basis of the criterion discussed in (Blake & Glazebrook 2003). In practice, we used $k_{\text{max}} = 0.145\, h\,\text{Mpc}^{-1}$, $0.18\, h\,\text{Mpc}^{-1}$, and $0.23\, h\,\text{Mpc}^{-1}$ for the redshifts $z = 0.5$, 1.0, and 1.5, respectively.

Figure 14 shows the result of the fit for one of these simulations. Figure 15 histogram show the recovered values of $k_{\text{BAO}\perp}$ and $k_{\text{BAO}\parallel}$ for 100 simulations. The widths of the two distributions give an estimate of the statistical errors.

In addition, in the fitting procedure, both the parameters modeling the signal A, τ, α, and the parameter correcting the noise power spectrum (a_0, a_1) are floated to take the possible ignorance of the signal shape and the uncertainties in the computation of the noise power spectrum into account. In this way, we can correct possible imperfections, and the systematic uncertainties are directly propagated to statistical errors on the relevant parameters $k_{\text{BAO}\perp}$ and $k_{\text{BAO}\parallel}$. By subtracting the fitted noise contribution to each simulation, the baryonic oscillations are clearly observed, for instance, in Fig. 16.

In our comparison of the various configurations, we have considered the following cases for $\Delta z = 0.5$ slices with $0.25 < z < 2.75$.

– *Simulation without electronics noise*: the statistical errors on the power spectrum are directly related to the number of modes in the surveyed volume V corresponding to the $\Delta z = 0.5$ slice with the solid angle $\Omega_{\text{tot}} = 1\,\pi$ sr. The number of modes $N_{\delta k}$ in the wave number interval δk can be written as

$$V = \frac{c}{H(z)}\Delta z \times (1 + z)^2 d_{\text{A}}^2 \Omega_{\text{tot}} \qquad N_{\delta k} = \frac{V}{4\pi^2}k^2 \delta k. \qquad (49)$$

– *Noise*: we add the instrument noise as a constant term P_{noise} as described in Eq. (32). Table 6 gives the white noise level for an $N = 400$ dish interferometer with $T_{\text{sys}} = 50$ K and one year total observation time to survey $\Omega_{\text{tot}} = 1\,\pi$ sr.
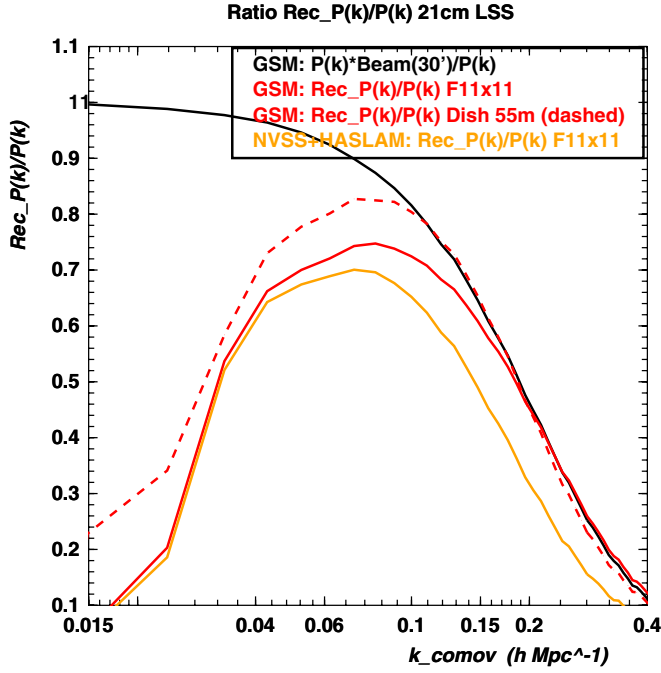
Fig. 12. Ratio of the reconstructed or extracted 21 cm power spectrum, after foreground removal, to the initial 21 cm power spectrum, $\mathbf{T}(k) = P_{21}^{\mathrm{rec}}(k)/P_{21}(k)$ (transfer function), at $z \sim 0.6$ for the instrument configuration (a), 11×11 packed array interferometer. The effect of a frequency-independent Gaussian beam of $\sim 30'$ is shown in black. The transfer function $\mathbf{T}(k)$ for the instrument configuration (a), 11×11 packed array interferometer, for the GSM/Model-I is shown in red, and in orange for Haslam+NVSS/Model-II. The transfer function for a $D = 55$ m diameter dish for the GSM model is also shown as the dashed red curve.
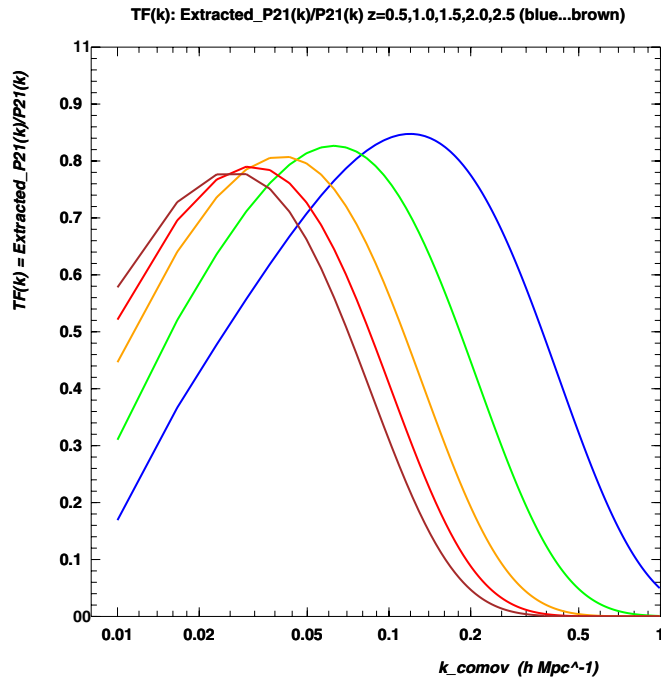

Fig. 13. Fitted/smoothed transfer function $\mathbf{T}(k)$ obtained for the recovered 21 cm power spectrum at different redshifts, $z = 0.5, 1.0, 1.5, 2.0, 2.5$ for the instrument configuration (e), 20×20 packed array interferometer.
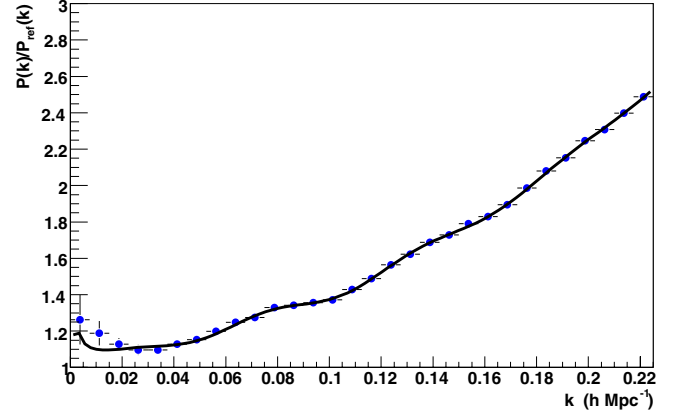

Fig. 14. 1D projection of the power spectrum for one simulation. The H_I power spectrum is divided by an envelop curve $P(k)_{\mathrm{ref}}$ corresponding to the power spectrum without baryonic oscillations. The dots represents one simulation for a "packed" array of dishes with a system temperature, $T_{\mathrm{sys}} = 50$ K, an observation time, $T_{\mathrm{obs}} = 1$ year, a solid angle of $1\pi sr$, an average redshift, $z = 1.5$ and a redshift depth, $\Delta z = 0.5$. The solid line is the result of the fit to the data.
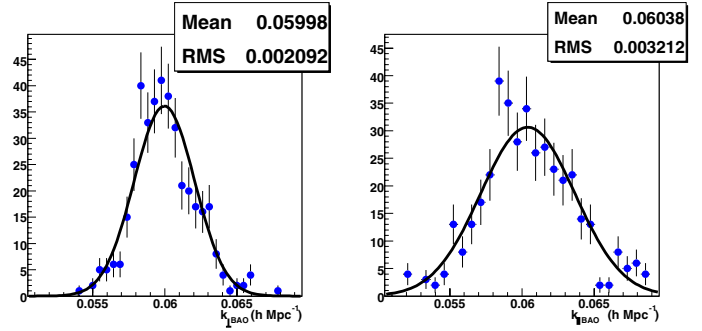

Fig. 15. Distributions of the reconstructed wavelength $k_{\mathrm{BAO}\perp}$ and $k_{\mathrm{BAO}\parallel}$ perpendicular and parallel, respectively, to the line of sight for simulations as in Fig. 14. The fit by a Gaussian of the distribution (solid line) gives the width of the distribution, which represents the statistical error expected on these parameters.
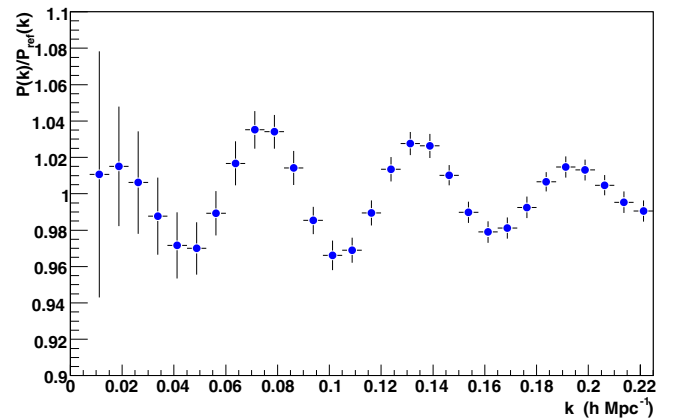

Fig. 16. 1D projection of the power spectrum averaged over 100 simulations of the packed dish array. The simulations are performed for the following conditions: a system temperature $T_{\mathrm{sys}} = 50$ K, an observation time $T_{\mathrm{obs}} = 1$ year, a solid angle of $1\pi sr$, an average redshift $z = 1.5$, and a redshift depth $\Delta z = 0.5$. The H_I power spectrum is divided by an envelop curve $P(k)_{\mathrm{ref}}$ corresponding to the power spectrum without baryonic oscillations, and the background estimated by a fit is subtracted. The errors are the rms of the 100 distributions for each k bin, and the dots are the mean of the distribution for each k bin.
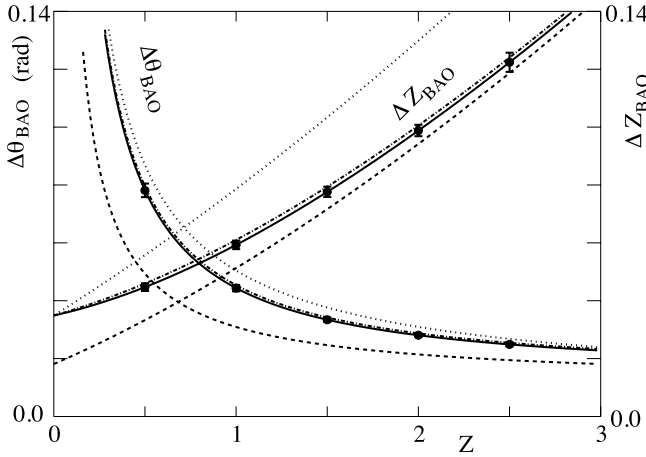
Fig. 17. The two "Hubble diagrams" for BAO experiments. The four falling curves give the angular size of the acoustic horizon (left scale) and the four rising curves give the redshift interval of the acoustic horizon (right scale). The solid lines are for $(\Omega_M, \Omega_\Lambda, w) = (0.27, 0.73, -1)$, the dashed for $(1, 0, -1)$ the dotted for $(0.27, 0, -1)$, and the dash-dotted for $(0.27, 0.73, -0.9)$, The error bars on the solid curve correspond to the four-month run (packed array) of Table 7.

Table 6. Noise spectral power.

z	0.5	1.0	1.5	2.0	2.5
P_{noise} mK^2 (Mpc^3/h)	8.5	35	75	120	170

– *Noise with transfer function*: we consider the interferometer response and radio foreground subtraction represented as the measured P(k) transfer function $T(k)$ (Sect. 4.3), as well as the instrument noise P_{noise}.

Table 7 summarizes the result. The errors both on $k_{\text{BAO}\perp}$ and $k_{\text{BAO}\parallel}$ decrease as a function of redshift for simulations without electronic noise because the volume of the universe probed is larger. Once we apply the electronics noise, each slice in redshift gives comparable results. Finally, after applying the full reconstruction of the interferometer, the best accuracy is obtained for the first slices in redshift around 0.5 and 1.0 for an identical time of observation. We can optimize the survey by using a different observation time for each slice in redshift. Finally, for a 3-year survey we can split in five observation periods with durations that are three months, three months, six months, one year and one year for redshift 0.5, 1.0, 1.5, 2.0, and 2.5, respectively (Table 7, 4th row).

5.2. Expected sensitivity on w_0 and w_a

The observations give the H$_I$ power spectrum in angle-angle-redshift space rather than in real space. The inverse of the peak positions in the observed power spectrum therefore gives the angular and redshift intervals corresponding to the sonic horizon. The peaks in the angular spectrum are proportional to $d_T(z)/a_s$ and those in the redshift spectrum to $d_H(z)/a_s$, where $a_s \sim 105 \, h^{-1}$ Mpc is the acoustic horizon comoving size at recombination, $d_T(z) = (1 + z)d_A$ is the comoving angular distance and $d_H = c/H(z)$ the Hubble distance (see Eq. (6)):

$$d_H = \frac{c}{H(z)} = \frac{c/H_0}{\sqrt{\Omega_\Lambda + \Omega_m(1+z)^3}} \qquad d_T = \int_0^z d_H(z)\mathrm{d}z. \qquad (50)$$

The quantities d_T, d_H, and a_s all depend on the cosmological parameters. Figure 17 gives the angular and redshift intervals as
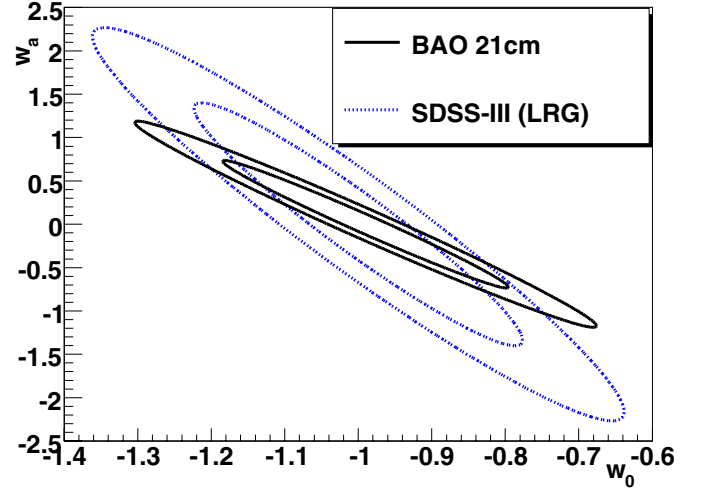
Fig. 18. 1σ and 2σ confidence level contours in the parameter plane (w_0, w_a), marginalized over all the other parameters, for two BAO projects: SDSS-III (LRG) project (blue dotted line), 21 cm project with HI intensity mapping (black solid line).

a function of redshift for four cosmological models. The error bars on the lines for $(\Omega_M, \Omega_\Lambda) = (0.27, 0.73)$ correspond to the expected errors on the peak positions taken from Table 7 for the four-month runs with the packed array. We see that with these uncertainties, the data would be able to measure w at better than the 10% level.

To estimate the sensitivity to parameters describing the dark energy equation of state, we follow the procedure explained in (Blake & Glazebrook 2003). We can introduce the equation of state of dark energy, $w(z) = w_0 + w_a \cdot z/(1 + z)$, by replacing Ω_Λ in the definition of $d_T(z)$ and $d_H(z)$, (Eq. (50)) by

$$\Omega_\Lambda \rightarrow \Omega_\Lambda \exp\left[3 \int_0^z \frac{1 + w(z')}{1 + z'} \mathrm{d}z'\right] \qquad (51)$$

where Ω_Λ^0 is the present-day dark energy fraction with respect to the critical density. Using the relative errors on $k_{\text{BAO}\perp}$ and $k_{\text{BAO}\parallel}$ given in Table 7, we can compute the Fisher matrix for five cosmological parameter: $(\Omega_m, \Omega_b, h, w_0, w_a)$. Then, the combination of this BAO Fisher matrix with the Fisher matrix obtained for Planck mission allows us to compute the errors on dark energy parameters. We used the Planck Fisher matrix, computed for the Euclid proposal (Laureijs 2009), for the 8 parameters: Ω_m, Ω_b, h, w_0, w_a, σ_8, n_s (spectral index of the primordial power spectrum) and τ (optical depth to the last-scatter surface), assuming a flat universe.

For an optimized project over a redshift range, $0.25 < z < 2.75$, with a total observation time of three years, the packed 400-dish interferometer array has a precision of 12% on w_0 and 48% on w_a. The figure of merit (FOM), the inverse of the area in the 95% confidence level contours, is 38. Finally, Fig. 18 shows a comparison of different BAO projects, with a set of priors on (Ω_m, Ω_b, h) corresponding to the expected precision on these parameters in early 2010s. The confidence contour level in the plane (w_0, w_a) were obtained by marginalizing over all the other parameters. This BAO project based on H$_I$ intensity mapping is clearly competitive with the current generation of optical surveys such as SDSS-III (Eisenstein et al. 2011).

Table 7. Sensitivity on k_{BAO} measurement.

z		0.5	1.0	1.5	2.0	2.5
No noise, pure cosmic variance	$\sigma(k_{BAO\perp})/k_{BAO\perp}$ (%)	1.8	0.8	0.6	0.5	0.5
	$\sigma(k_{BAO\parallel})/k_{BAO\parallel}$ (%)	3.0	1.3	0.9	0.8	0.8
Noise without transfer function (a)	$\sigma(k_{BAO\perp})/k_{BAO\perp}$ (%)	2.3	1.8	2.2	2.4	2.8
(3-months/redshift bin)	$\sigma(k_{BAO\parallel})/k_{BAO\parallel}$ (%)	4.1	3.1	3.6	4.3	4.4
Noise with transfer function (a)	$\sigma(k_{BAO\perp})/k_{BAO\perp}$ (%)	3.0	2.5	3.5	5.2	6.5
(3-months/redshift bin)	$\sigma(k_{BAO\parallel})/k_{BAO\parallel}$ (%)	4.8	4.0	6.2	9.3	10.3
Optimized survey (b)	$\sigma(k_{BAO\perp})/k_{BAO\perp}$ (%)	3.0	2.5	2.3	2.0	2.7
(Observation time: 3 years)	$\sigma(k_{BAO\parallel})/k_{BAO\parallel}$ (%)	4.8	4.0	4.1	3.6	4.3

Notes. Relative errors on $k_{BAO\perp}$ and $k_{BAO\parallel}$ measurements are given as a function of the redshift z for various simulation configurations: [a] simulations with electronics noise, without (2nd row) and with (3rd row) the transfer function; [b] optimized survey, simulations with electronic noise and the transfer function.

6. Conclusions

The 3D mapping of redshifted 21 cm emission through *intensity mapping* is a novel and complementary approach to optical surveys for studying the statistical properties of the LSS in the universe up to redshifts $z \lesssim 3$. A radio instrument with a large, instantaneous FOV (10–100 deg^2) and large bandwidth ($\gtrsim$100 MHz) with ~10 arcmin resolution is needed to perform a cosmological neutral hydrogen survey over a significant fraction of the sky. We have shown that a nearly packed interferometer array with a few hundred receiver elements spread over an hectare or a hundred beam focal plane array with a ~100 m primary reflector will have the required sensitivity to measure the 21 cm power spectrum. A method of computing the instrument response for interferometers was developed, and we computed the noise power spectrum for various telescope configurations. The Galactic synchrotron and radio sources are a thousand times brighter than the redshifted 21 cm signal, making the measurement of the latter signal a major scientific and technical challenge. We also studied the performance of a simple foreground subtraction method through realistic models of the sky emissions in the GHz domain and simulation of interferometric observations. We were able to show that the cosmological 21 cm signal from the LSS should be observable, but requires a very good knowledge of the instrument response. Our method allowed us to define and compute the overall *transfer function* or *response function* for the measurement of the 21 cm power spectrum. Finally, we used the computed noise power spectrum and $P(k)$ measurement response function to estimate the precision on the determination of dark energy parameters, for a 21 cm BAO survey. This radio survey could be carried out using the current technology and would be competitive with the ongoing or planned optical surveys for dark energy, with a fraction of their cost.

References

Abdalla, F. B., & Rawlings, S. 2005, MNRAS, 360, 27
Abell, P. A., Allison, J., Anderson, J. F., et al. 2009, LSST Science book [arXiv:0912.0201]
Albrecht, A., Bernstein, G., Cahn, R., et al. 2006, Dark Energy Task Force [arXiv:astro-ph/0609591]
Ansari, R., Le Goff, J.-M., Magneville, C., et al. 2008, unpublished [arXiv:0807.3614]
Barkana, R., & Loeb, A. 2007, Rep. Prog. Phys, 70, 627
Blake, C., & Glazebrook, K. 2003, ApJ, 594, 665
Blake, C., Davis, T., Poole, G. B., et al. 2011, MNRAS, 415, 2892
Binney, J., & Merrifield, M. 1998, Galactic Astronomy (Princeton University Press)
Bowman, J. D., Morales, M. F., & Hewitt, J. N. 2006, ApJ, 638, 20
Bowman, J. D., Barnes, D. G., Briggs, F. H., et al. 2007, AJ, 133, 1505
Bowman, J. D., Morales, M., & Hewitt, J. N. 2009, ApJ, 695, 183

Carilli, C., & Rawlings, S. 2004, Science with the Square Kilometre Array, New Astron. Rev., 48
Chang, T., Pen, U.-L., Peterson, J. B., & McDonald, P. 2008, Phys. Rev. Lett., 100, 091303
Chang, T.-C., Pen, U.-L., Bandura, K., & Peterson, J. B. 2010, Nature, 466, 463
Cole, S., Percival, W. J., Peacock, J. A., et al. 2005, MNRAS, 362, 505
Condon, J. J., Cotton, W. D., Greisen, E. W., et al. 1998, AJ, 115, 1693
Di Matteo, T., Perna, R., Abel, T., & Rees, M. J. 2002, ApJ, 564, 576
Eisenstein, D., & Hu, W. 1998, ApJ, 496, 605
Eisenstein, D. J., Zehavi, I., Hogg, D. W., et al. 2005, ApJ, 633, 560
Eisenstein, D. J., Weinberg, D. H., Agol, E., et al. 2011, AJ, 142, 72
Field, G. B. 1959, ApJ, 129, 155
Furlanetto, S., Peng Oh, S., & Briggs, F. 2006, Phys. Rep., 433, 181
Ghosh, A., Bharadwaj, S., Ali, Sk. S., & Chengalur, J. N. 2011, MNRAS, 411, 2426
Glazebrook, K., & Blake, C. 2005, ApJ, 631, 1
Haslam, C. G. T., Salter, C. J., Stoffel, H., & Wilson, W. E. 1982, A&AS, 47, 1
Jackson, C. A. 2004, New A, 48, 1187
Komatsu, E., Smith, K. M., Dunkley, J., et al. 2011, ApJS, 192, 18
Lah, P., Pracy, M. B., Chengalur, J. N., et al. 2009, MNRAS, 399, 1447
Lang, K. R. 1999, Astrophysical Formulae, 3rd edn. (Springer)
Larson, D., Dunkley, J., Hinshaw, G., et al. (WMAP) 2011, ApJS, 192, 16
Lonsdale, C. J., Cappallo, R. J., Morales, M. F., et al. 2009, IEEE Proc., 97, 1497 [arXiv:0903.1828]
Laureijs, R. 2009 [arXiv:0912.0914]
Madau, P., Meiksin, A., & Rees, M. J. 1997, ApJ, 475, 429
McDonald, P., & Eisenstein, D. J. 2007, Phys. Rev. D 76, 6, 063009
McDonald, P., Seljak, U., Burles, S., et al. 2006, ApJS, 163, 80
Mauskopf, P. D., Ade, P. A. R., de Bernardis, P., et al. 2000, ApJ, 536, 59
McQuinn, M., Zahn, O., Zaldarriaga, M., Hernquist, L., & Furlanetto, S. R. 2006, ApJ, 653, 815
Morales, M., & Hewitt, J. 2004, ApJ, 615, 7
Morales, M., Bowman, J. D., & Hewitt, J. N. 2006, ApJ, 648, 767
Oh, S. P., & Mack, K. J. 2003, MNRAS, 346, 871
de Oliveira-Costa, A., Tegmark, M., Gaensler, B. M., et al. 2008, MNRAS, 388, 247
Parsons, A. R., Backer, D. C., Bradley R. F., et al. 2010, AJ, 139, 1468
Peebles, P. J. E. 1993, Principles of Physical Cosmology (Princeton University Press)
Peterson, J. B., Bandura, K., & Pen, U.-L. 2006, unpublished [arXiv:astro-ph/0606104]
Platania, P., Bensadoun, M., Bersanelli, M., et al. 1998, ApJ, 505, 473
Percival, W. J., Nichol, R. C., Eisenstein, D. J., et al. 2007, ApJ, 657, 645
Percival, W. J., Reid, B. A., Eisenstein, D. J., et al. 2010, MNRAS, 401, 2148
James, R. 2001, Fundamentals of Cosmology (Springer)
Rogers, A. E. E., & Bowman, J. D. 2008, AJ, 136, 641
Rottgering, H. J. A., Braun, R., Barthel, P. D., et al. 2006, Proc. Conf. Cosmology, galaxy formation and astroparticle physics on the pathway to the SKA, Oxford, April 2006 [arXiv:astro-ph/0610596]
Shaver, P. A., Windhorst, R. A., Madau, P., & de Bruyn, A. G. 1999, A&A, 345, 380
Seo, H. J., Dodelson, S., Marriner, J., et al. 2010, ApJ, 721, 164
Tegmark, M., & Zaldarriaga, M. 2009, Phys. Rev. D, 79, 8
Tegmark, M., Blanton, M. R., Strauss, M. A., et al. 2004, ApJ, 606, 702
Thompson, A. R., Moran, J. M., & Swenson, G. W. 2001, Interferometry and Synthesis in Radio Astronomy, 2nd edn. (John Wiley & sons)
Wolfe, A. M., Gawiser, E., & Prochaska, J. X. 2005 ARA&A, 43, 861
Wyithe, S., Loeb, A., & Geil, P. 2008, MNRAS, 383, 1195
Zaldarriaga, M., Furlanetto, S. R., & Hernquist, L. 2004, ApJ, 608, 622
Zwaan, M. A., Meyer, M. J., Staveley-Smith, L., & Webster, R. L. 2005, MNRAS, 359, L30